Research Paper

GEOSPHERE

GEOSPHERE, v. 18, no. 1

https://doi.org/10.1130/GES02386.1

11 figures; 3 tables; 2 sets of supplemental files

CORRESPONDENCE: nolan.blackford@wsu.edu

CITATION: Blackford, N.R., Long, S.P., Stout, A., Rodgers, D.W., Cooper, C.M., Kramer, K., Di Fiori, R.V., and Soignard, E., 2021, Late Cretaceous upper-crustal thermal structure of the Sevier hinterland: Implications for the geodynamics of the Nevadaplano: Geosphere, v. 18, no. 1, p. 183–210, https://doi.org/10.1130/GES02386.1.

Science Editor: Andrea Hampel
Associate Editor: Francesco Mazzarini

Received 14 December 2020
Revision received 11 May 2021
Accepted 8 July 2021

Published online 22 November 2021

Late Cretaceous upper-crustal thermal structure of the Sevier hinterland: Implications for the geodynamics of the Nevadaplano

Nolan R. Blackford[1], Sean P. Long[1], Austin Stout[1], David W. Rodgers[2], C.M. Cooper[1], Kimberly Kramer[1], Russell V. Di Fiori[1,3], and Emmanuel Soignard[4]

[1]School of the Environment, Washington State University, Pullman, Washington 99164, USA
[2]Department of Geosciences, Idaho State University, Pocatello, Idaho 83209, USA
[3]Idaho Geological Survey, University of Idaho, Moscow, Idaho 83844, USA
[4]Eyring Materials Center, Arizona State University, Tempe, Arizona 85287, USA

ABSTRACT

Crustal temperature conditions can strongly influence the evolution of deformation during orogenesis. The Sevier hinterland plateau in Nevada and western Utah ("Nevadaplano") experienced a Late Cretaceous episode of shallow-crustal metamorphism and granitic magmatism. Here, we investigate the thermal history of the Nevadaplano by measuring peak thermal field gradients attained in the upper 10–20 km of the crust along an east-west transect through nine ranges in eastern Nevada and western Utah, by integrating Raman spectroscopy of carbonaceous material thermometry and published conodont alteration indices with reconstructed cross sections. Thermal field gradients of 29 ± 3 °C/km were obtained in the House and Confusion Ranges in westernmost Utah. The Deep Creek, Schell Creek, and Egan Ranges in easternmost Nevada yielded elevated gradients of 49 ± 7 °C/km, 36 ± 3 °C/km, and 32 ± 6 °C/km, respectively. Moving westward, the White Pine, Butte, Pancake, and Fish Creek Ranges exhibit gradients typically between ~20–30 °C/km. The elevated thermal gradients in easternmost Nevada are interpreted to have been attained during ca. 70–90 Ma granitic magmatism and metamorphism and imply possible partial melting at ~18 km depths. Our data are compatible with published interpretations of Late Cretaceous lithospheric mantle delamination under the Sevier hinterland, which triggered lower-crustal anatexis and the resulting rise of granitic melts. The lack of evidence for structures that could have accommodated deep burial of rocks in the nearby Northern Snake Range metamorphic core complex, combined with thermal gradients from adjacent ranges that are ~1.5–3 times higher than those implied by thermobarometry in the Northern Snake Range, further highlights the debate over possible tectonic overpressure in Cordilleran core complexes. Cross-section retro-deformation defines 73.4 ± 4.6 km (76 ± 8%) of extension across eastern Nevada and 15 km of shortening in the Eastern Nevada fold belt.

1. INTRODUCTION

The thermal architecture of an orogenic belt can exert a first-order control on the style, magnitude, location, and dynamics of deformation (e.g., Royden, 1993; Henry et al., 1997; Huerta et al., 1998; Beaumont et al., 2001; Wells and Hoisch, 2008; Kohn, 2014). Therefore, quantifying the thermal conditions within orogenic crust can provide important insights into the processes that accommodate crustal thickening, contribute to the construction of orogenic plateaus, and dictate thrust belt dynamics (e.g., England and Thompson, 1984; Dahlen, 1990; Rahl et al., 2005; Hyndman and Currie, 2011; Kohn, 2016).

The Jurassic–Paleogene Cordilleran orogenic belt, which was constructed as a consequence of Andean-style subduction on the western margin of the North American plate, experienced a ~100 m.y. history of crustal shortening, magmatism, and metamorphism (e.g., Allmendinger, 1992; Burchfiel et al., 1992; DeCelles, 2004; Yonkee and Weil, 2015). In the portion of the Cordilleran orogen at the latitude of Nevada and Utah (Fig. 1), a high-elevation retroarc plateau (or "Nevadaplano") is interpreted to have developed in eastern Nevada and westernmost Utah by the late stages of shortening in the Late Cretaceous–early Paleogene (e.g., Coney and Harms, 1984; DeCelles, 2004; Cassel et al., 2014; Snell et al., 2014; Chapman et al., 2015; Long, 2019). During the Late Cretaceous (ca. 70–90 Ma), the Nevadaplano experienced a tectonothermal episode, which resulted in variably distributed greenschist- to amphibolite-facies metamorphism and granitic magmatism at upper-crustal levels (e.g., Barton et al., 1988; Miller et al., 1988; Miller and Gans, 1989; Barton, 1990; Long and Soignard, 2016) (Fig. 1). This event has been interpreted as the shallow thermal expression of an episode of lower-crustal anatexis, which resulted in the upward rise of granitic crustal melts (e.g., Barton, 1987, 1990; Miller et al., 1988; Miller and Gans, 1989; Wells and Hoisch, 2008). However, hypotheses for the genesis of Late Cretaceous anatexis differ and include heat influx following delamination of mantle lithosphere (Wells and Hoisch, 2008; Wells et al., 2012) or relaxation of isotherms within recently thickened crust (Miller and Gans, 1989).

The primary goal of this study is to elucidate the thermal history of the Nevadaplano by quantifying the magnitude and spatial distribution of anomalous upper-crustal heating associated with this Late Cretaceous magmatic-metamorphic episode. To accomplish this, we measure the peak temperature conditions attained in the upper crust along a ~300 km east-west transect through eastern Nevada and western Utah; this transect spans nine mountain ranges (Fig. 1). To quantify peak thermal gradients in each range,

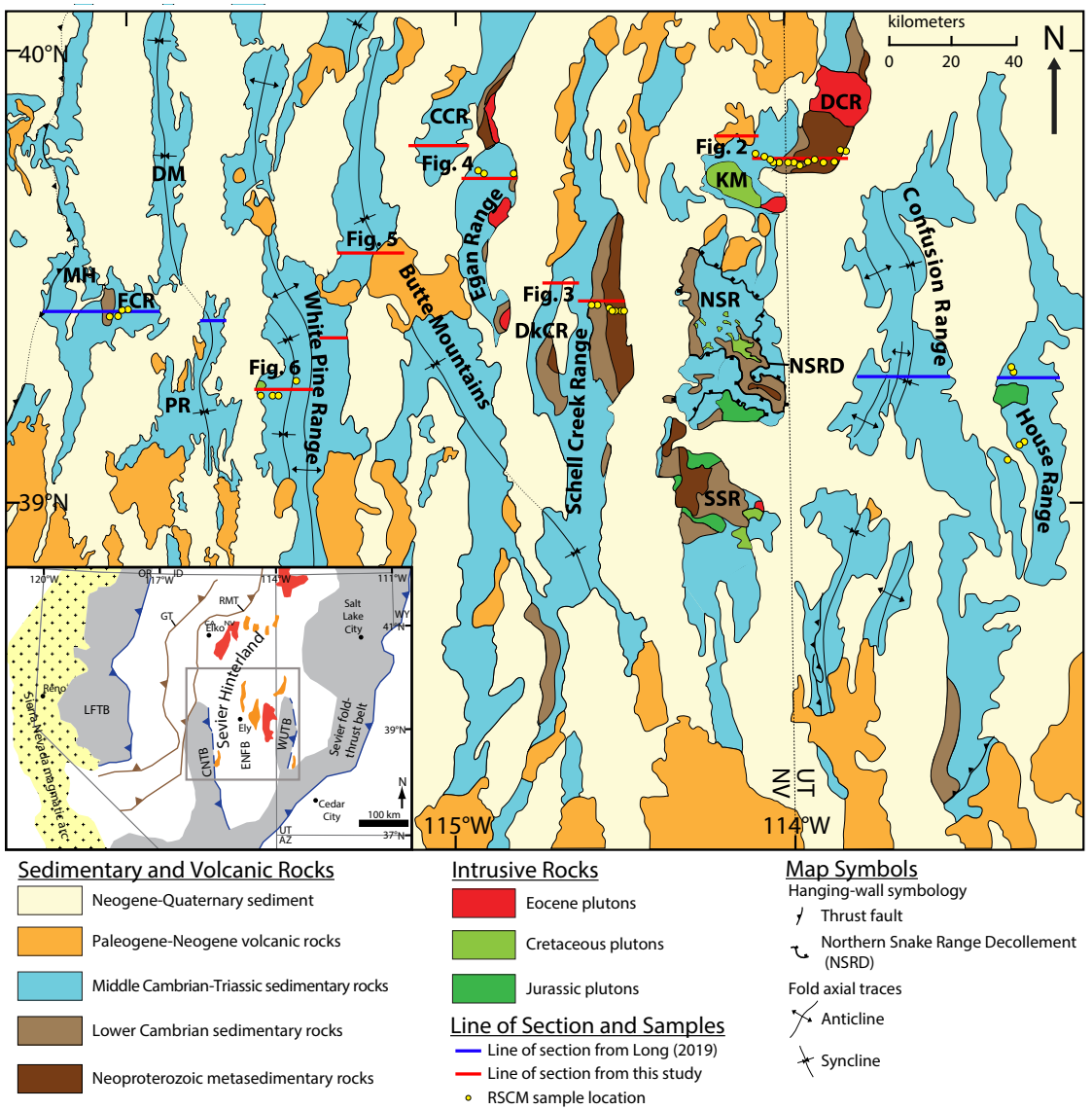

Figure 1. Simplified geologic map of east-central Nevada and west-central Utah, modified from Lee et al. (2017). Lines of section from this study are shown in red; lines of section from Long (2019) are shown in blue; and Raman spectroscopy of carbonaceous material (RSCM) samples are shown as yellow dots. Abbreviations: CCR—Cherry Creek Range; DCR—Deep Creek Range; DkCR—Duck Creek Range; DM—Diamond Mountains; FCR—Fish Creek Range; KM—Kern Mountains; MH—Mahogany Hills; NSR—Northern Snake Range; PR—Pancake Range; SSR—Southern Snake Range. Map inset on lower left (modified from Long and Soignard, 2016) shows Paleozoic thrust systems in brown and the deformation fronts of Mesozoic Cordilleran thrust systems in blue (with their approximate spatial extents shaded gray). Core complexes are shown in red, and areas of exposed Mesozoic metasedimentary rocks are shown in orange. Inset abbreviations: AZ—Arizona; CA—California; CNTB—Central Nevada thrust belt; ENFB—Eastern Nevada fold belt; GT—Golconda thrust; ID—Idaho; LFTB—Luning-Fencemaker thrust belt; NV—Nevada; OR—Oregon; RMT—Roberts Mountains thrust; UT—Utah, WUTB—Western Utah thrust belt; WY—Wyoming.

we integrate Raman spectroscopy of carbonaceous material thermometry and the exceptional conodont alteration index data sets of Harris et al. (1980) and Crafford (2007) with cross sections that we reconstruct for Cenozoic extension. We take advantage of the Cenozoic extensional dismemberment of the Nevadaplano, which allows us to collect data from paleo-depths as great as ~20 km. We then interpret our results in the context of the differing published hypotheses for the geodynamics of the Cordilleran orogen during the Late Cretaceous, including the delamination model of Wells and Hoisch (2008), and we explore implications for the processes that drove heat transfer in the Nevadaplano. We also examine the implications of our data for long-standing disagreements that imply high-magnitude structural burial and low geothermal gradients, versus regional field observations that indicate minimal structural burial and high geothermal gradients in Cordilleran core complexes. Finally, we present new estimates of total Cenozoic extension and total Cordilleran shortening across eastern Nevada, and we explore implications for pre-extensional crustal thickness and dominant thickening mechanisms.

2. GEOLOGIC FRAMEWORK

From the late Neoproterozoic to the Devonian, eastern Nevada and western Utah were situated on the western, passive margin of Laurentia, which was the site of deposition of up to ~10 km of shallow-marine clastic and carbonate sediments (e.g., Stewart and Poole, 1974; Stewart, 1980; Poole et al., 1992). During the Mississippian Antler orogeny, deep marine sedimentary rocks were thrust eastward over sedimentary rocks of the continental shelf in central Nevada, contemporaneous with deposition of clastic sediments in a foreland basin in eastern Nevada (e.g., Nolan et al., 1974; Speed and Sleep, 1982; Burchfiel et al., 1992; Poole et al., 1992; Dickinson, 2004, 2006). Following the Antler orogeny, shallow-marine, carbonate-dominated sedimentation continued until the Triassic (e.g., Stewart, 1980).

During the Jurassic, the development of an Andean-style subduction zone on the western margin of North America initiated the construction of the Cordilleran orogen (e.g., Allmendinger, 1992; Burchfiel et al., 1992; DeCelles, 2004; Dickinson, 2004; Yonkee and Weil, 2015). The majority of Cordilleran upper-crustal shortening (~200 km) was accommodated in the east-vergent Sevier fold-thrust belt in western Utah and southern Nevada (Fig. 1) between the Late Jurassic and the Paleogene (ca. 160–50 Ma) (e.g., DeCelles, 2004; Yonkee and Weil, 2015; Giallorenzo et al., 2018). To the west of the Sevier fold-thrust belt, a broad region of the Cordilleran retroarc in eastern Nevada and westernmost Utah is often referred to as the "Sevier hinterland" (e.g., Armstrong, 1972). Upper-crustal shortening, though likely of a low magnitude (a few tens of km), was diffusely distributed across the Sevier hinterland, and it was accommodated by east-vergent thrust systems in central Nevada and western Utah and a broad region of open folds in eastern Nevada (e.g., Gans and Miller, 1983; Taylor et al., 2000; Long, 2012, 2015; Greene, 2014; Long et al., 2014a, 2014b; Di Fiori et al., 2020) (Fig. 1). By the late stages of Cordilleran shortening in the Late Cretaceous–Paleogene, the Sevier hinterland in eastern Nevada is interpreted to have been a high-elevation (~2.2–3.5 km) plateau ("Nevadaplano"), which was underlain by ~50–60-km-thick crust (e.g., Coney and Harms, 1984; Allmendinger, 1992; DeCelles, 2004; Cassel et al., 2014; Snell et al., 2014; Chapman et al., 2015; Long, 2019).

During Cordilleran orogenesis, eastern Nevada and western Utah experienced two episodes of upper-crustal granitic magmatism and associated metamorphism. The first occurred during the Jurassic (ca. 155–165 Ma) and is characterized by isolated intrusions with proximal contact metamorphism (e.g., Barton et al., 1988; Miller et al., 1988; Miller and Hoisch, 1995; Zuza et al., 2020a). The second episode occurred during the Late Cretaceous (ca. 70–90 Ma) and was more regionally significant in east-central Nevada, resulting in emplacement of spatially isolated but broadly distributed intrusions at middle- and upper-crustal levels (e.g., Barton et al., 1988; Fryxell, 1988; Miller et al., 1988; Miller and Gans, 1989; Barton, 1990; Long and Soignard, 2016). The peak thermal conditions attained in the upper crust in eastern Nevada, as recorded by greenschist- to amphibolite-facies metamorphism in Neoproterozoic to Lower Cambrian sedimentary rocks that have been exhumed from paleo-depths of ~8–14 km in several ranges, are interpreted to have been achieved during this Late Cretaceous magmatic episode (Miller et al., 1988; Miller and Gans, 1989; Barton, 1990; Cooper et al., 2010). Late Cretaceous magmatism has been interpreted as the upper-crustal expression of lower-crustal anatexis, triggered either by heat influx following lithospheric delamination (Wells and Hoisch, 2008; Wells et al., 2012) or by conductive relaxation of isotherms in structurally thickened crust (Miller and Gans, 1989).

During the Paleocene and Eocene, the Cordilleran deformation front migrated eastward into Utah and Colorado, constructing the Laramide province, which is interpreted as the result of shallowing of the subduction angle (e.g., Dickinson and Snyder, 1978; Dickinson, 2006). Following this, between the late Eocene and early Miocene, silicic volcanism swept from the northeast to southwest across western Utah and Nevada during the Great Basin ignimbrite flare-up (e.g., Best et al., 2009; Henry and John, 2013) and has been interpreted as the consequence of slab rollback (Humphreys, 1995; Dickinson, 2002; Smith et al., 2014). Volcanic rocks of the ignimbrite flare-up were deposited on deformed Paleozoic–Mesozoic sedimentary rocks, defining an orogen-wide erosion surface (referred to here as the "Paleogene unconformity") that postdates Cordilleran shortening but predates nearly all extensional tectonism (e.g., Armstrong, 1972; Gans and Miller, 1983; Long, 2012, 2019). Following (and in some places temporally overlapping with) the ignimbrite flare-up, Nevada and western Utah transitioned into an extensional regime, with localized late Eocene–Oligocene extension in eastern Nevada (e.g., Gans and Miller, 1983; Gans et al., 2001; Lee et al., 2017; Long et al., 2018). The widespread extension that formed the Basin and Range Province began in the middle Miocene (e.g., Dickinson, 2002; Colgan and Henry, 2009) and is attributed to the reorganization of the western North American margin from a subduction zone to a transform boundary (e.g., Atwater, 1970; Dickinson, 2002).

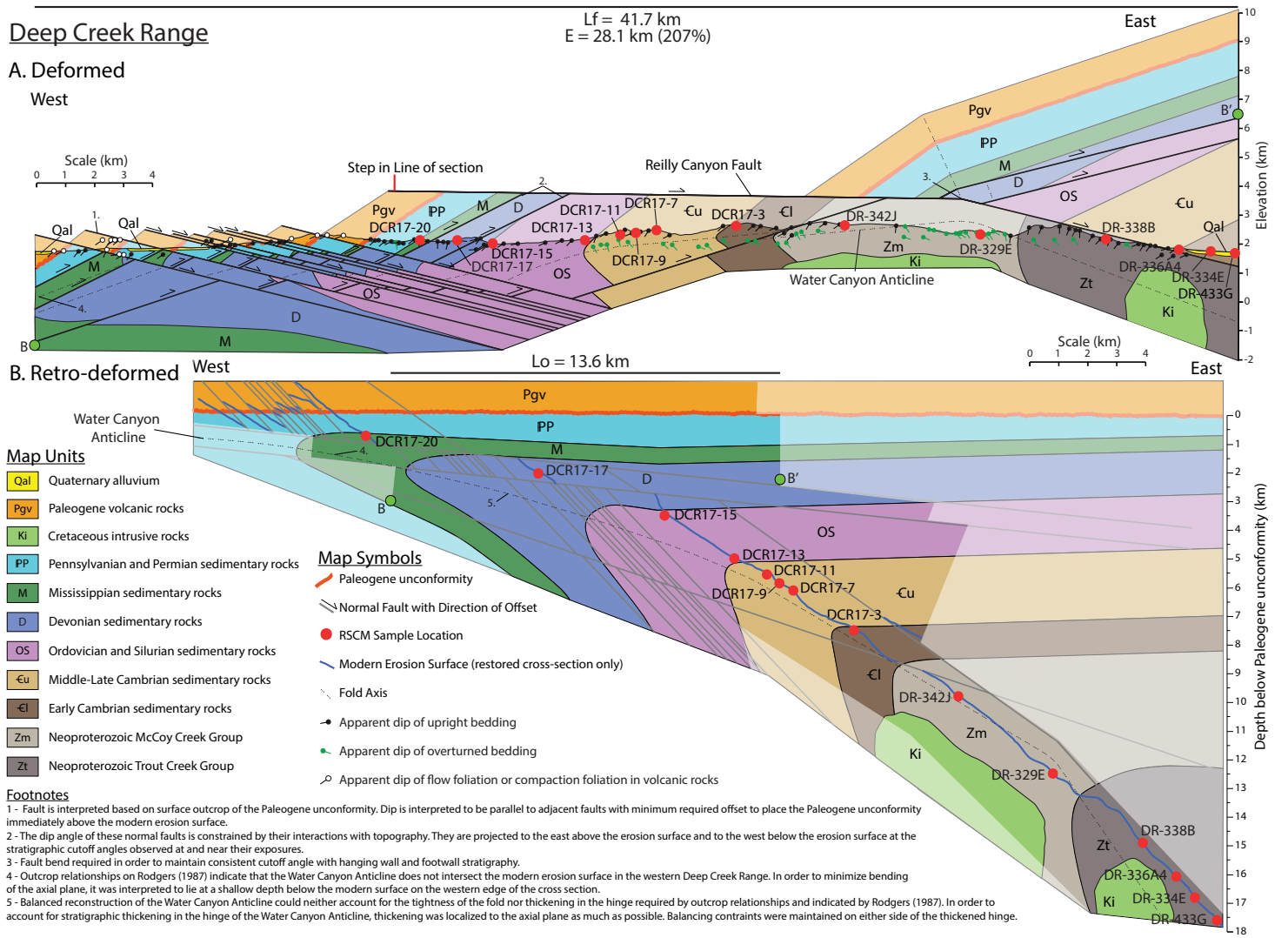

Figure 2. Cross sections of the Deep Creek Range. (A) Deformed cross section with present-day geometry based on the mapping of Rodgers (1987). Translucent area above the modern erosion surface represents eroded rocks. (B) Cross section retro-deformed to its pre-extensional geometry. Translucent areas represent rocks that restore outside of the area shown on A. Line lengths L_f and L_o were measured between reference points B and B′ (green dots).

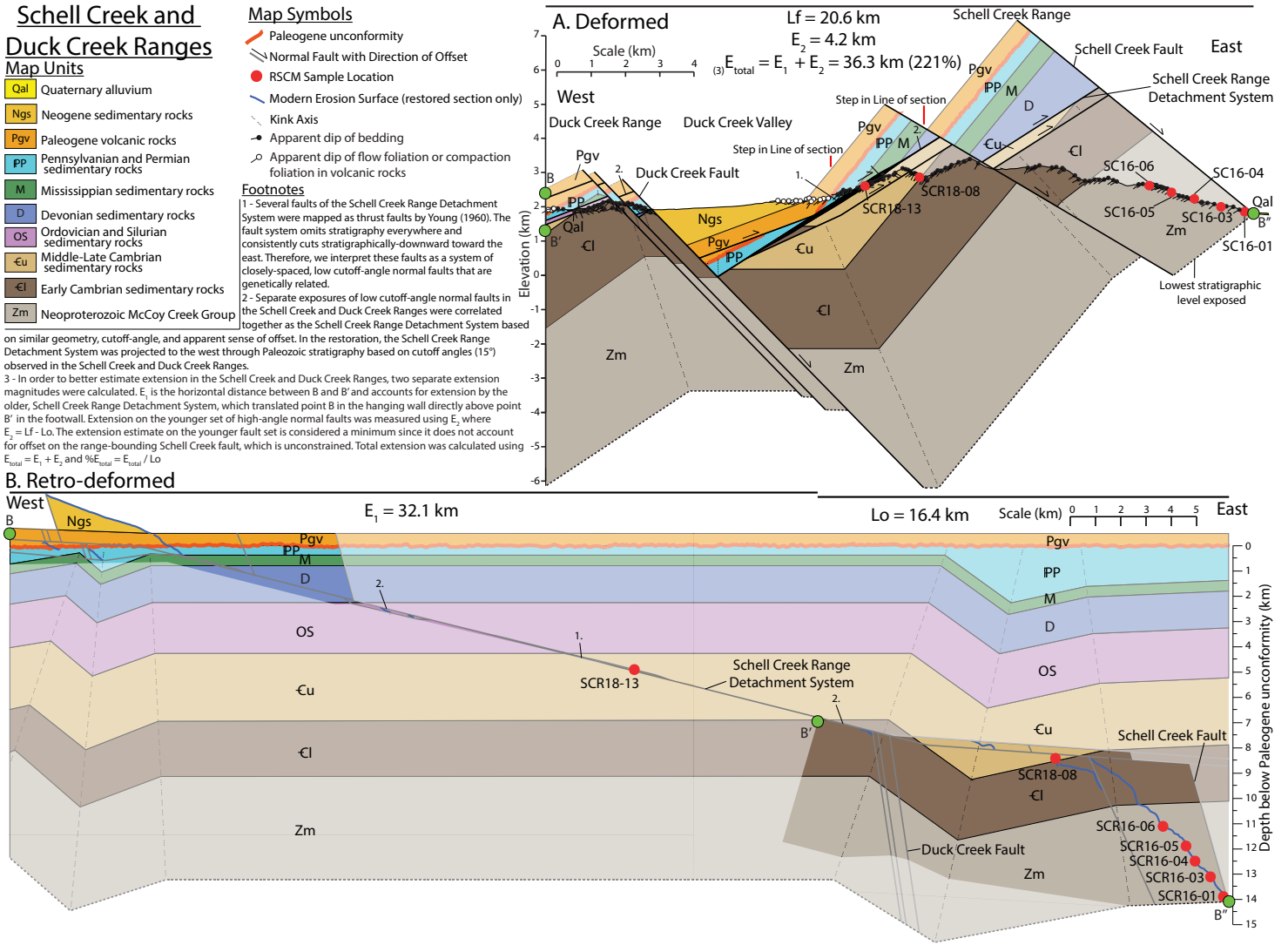

Figure 3. (A) Deformed (based on the mapping of Young [1960] and Gans et al. [1985]) and (B) retro-deformed cross sections of the Schell Creek and Duck Creek Ranges. Note that the deformed and restored cross sections are shown at different scales. Line lengths L_f, L_o, and E_1 were measured between reference points B, B′, and B″ (green dots).

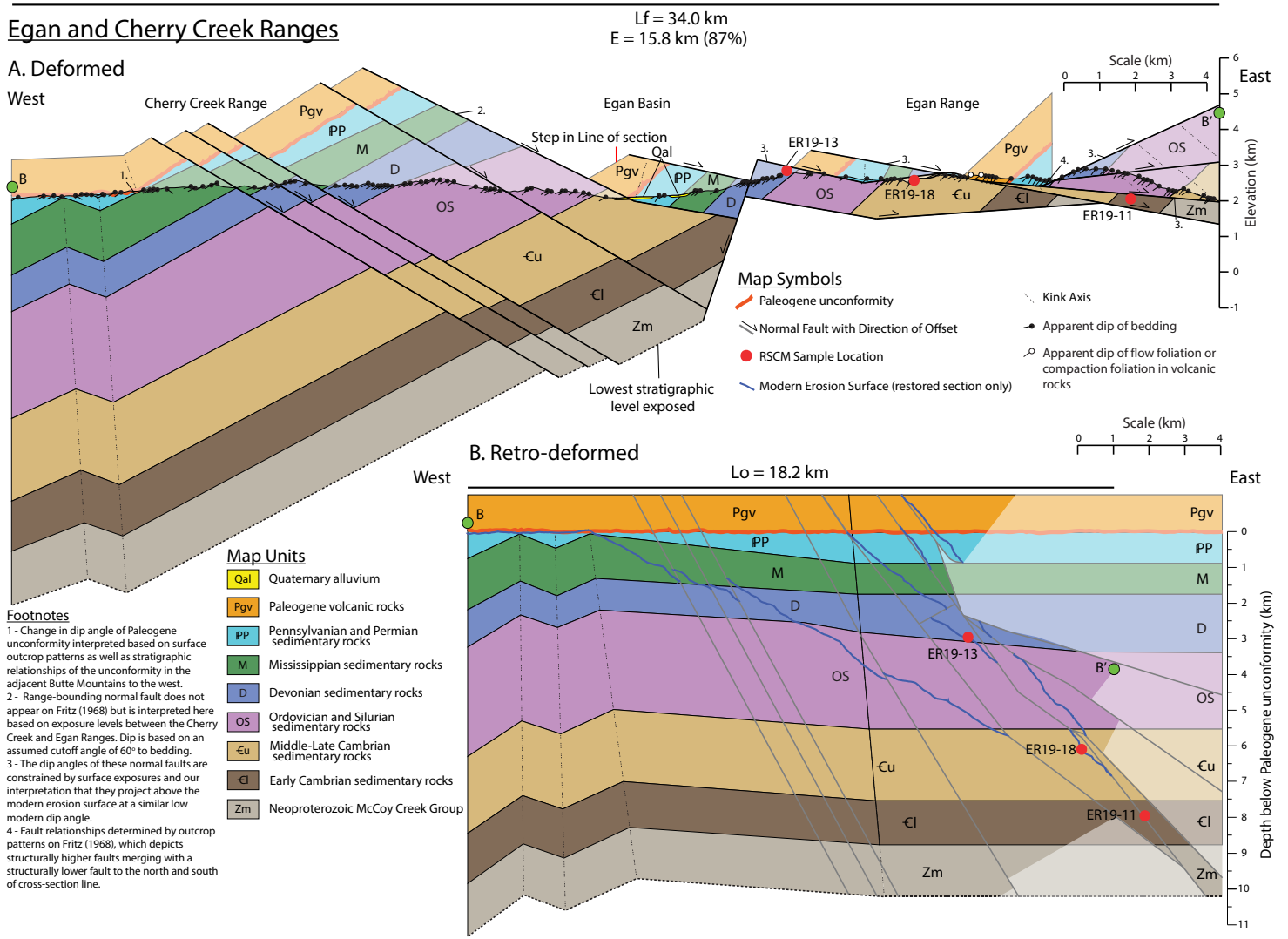

Figure 4. (A) Deformed (based on the mapping of Fritz, 1968) and (B) retro-deformed cross sections of the Egan and Cherry Creek Ranges. Line lengths L_f and L_o were measured between reference points B and B′ (green dots).

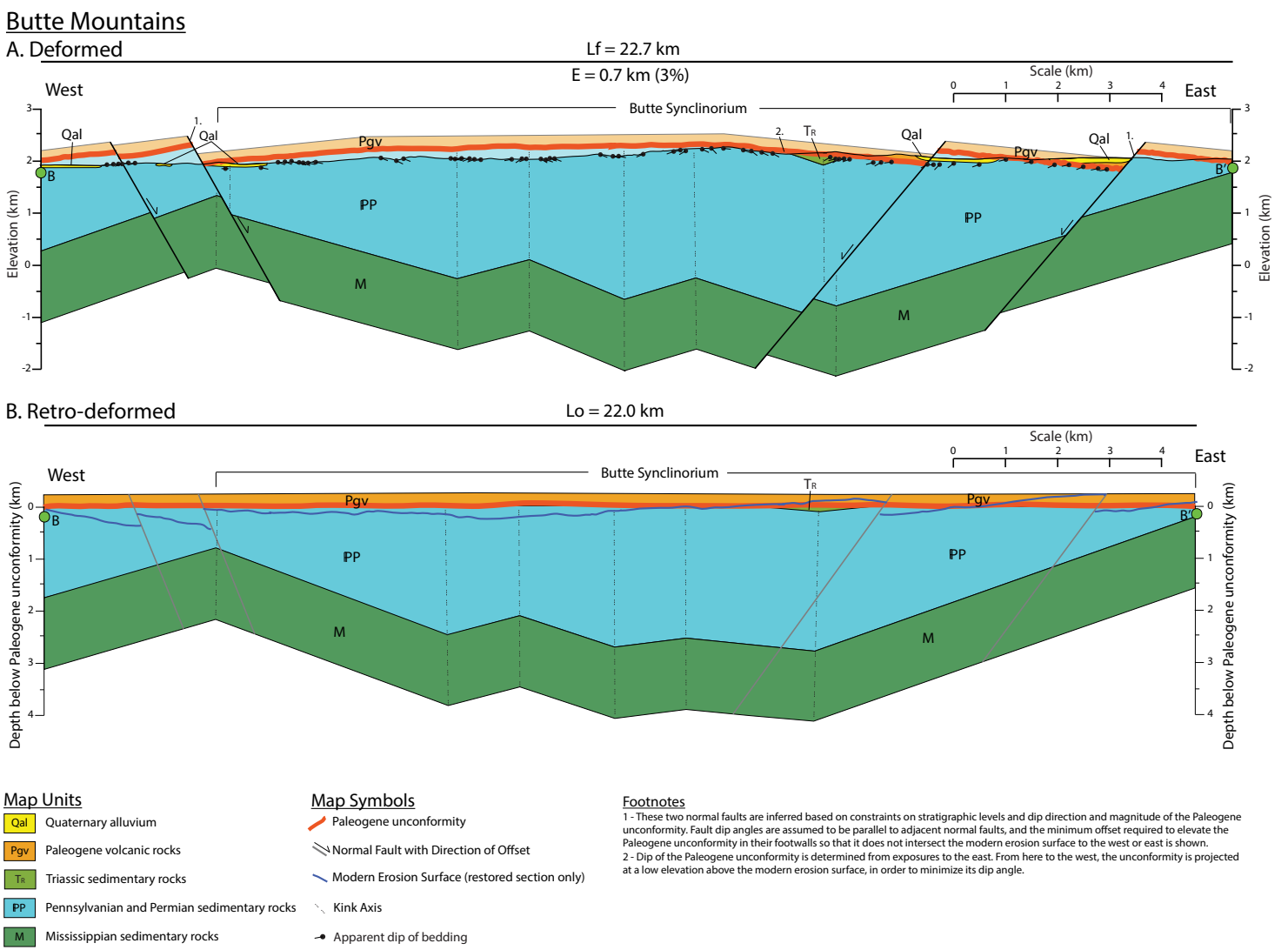

Figure 5. (A) Deformed (based on the mapping of Douglass, 1960) and (B) retro-deformed cross sections of the Butte Mountains. Line lengths L_f and L_o were measured between reference points B and B′ (green dots).

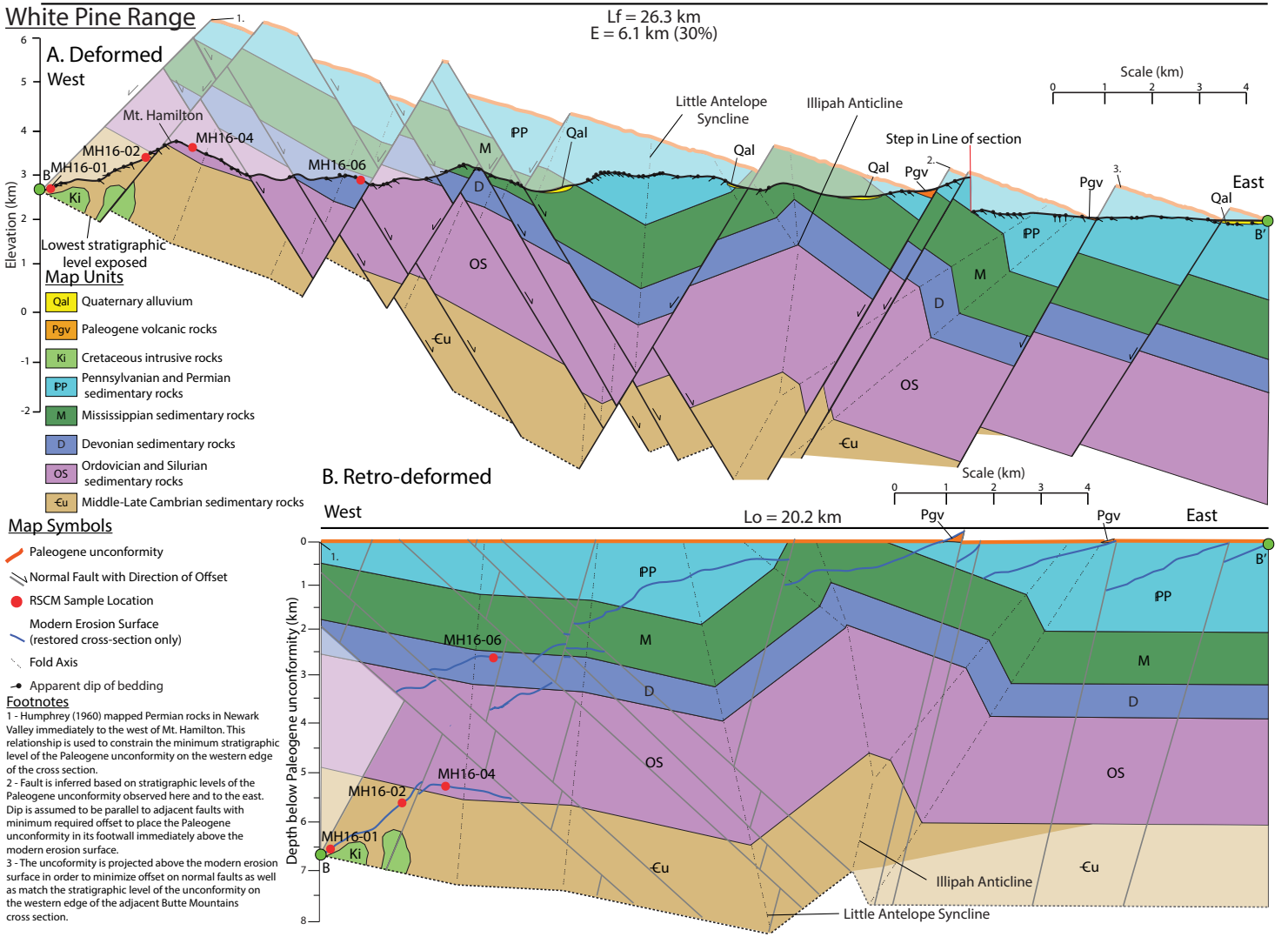

Figure 6. (A) Deformed (based on the mapping of Humphrey, 1960) and (B) retro-deformed cross sections of the White Pine Range. Line lengths L_f and L_o were measured between reference points B and B′ (green dots).

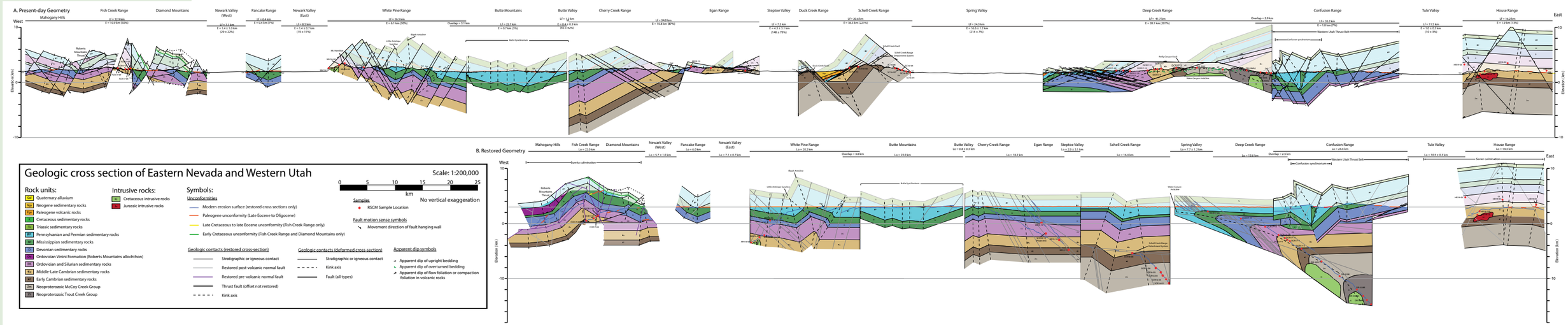

To view Figure 7 at full size, please visit https://doi.org/10.1130/GEOS.S.16984726 or access the full-text article on www.gsapubs.org.

Figure 7. Compilation of cross sections across east-central Nevada and western Utah (1:200,000 scale) with deformed cross sections in the top row (A) and restored cross sections in the bottom row (B). Translucent areas represent eroded rock above the modern surface (deformed cross sections) and above the Paleogene unconformity (restored cross sections). Locations of the lines of section and Raman spectroscopy of carbonaceous material (RSCM) samples are shown on Figure 1. Extension accommodated in valleys was approximated by averaging the percent extension of the ranges on either side, and assigning an uncertainty based on the difference in percent extension, after the methods described in Long (2019) (for example, a valley bounded by ranges with extension magnitudes of 20% and 30% was interpreted to have experienced 25 ± 5% extension; the basin was then retro-deformed accordingly, and an uncertainty was calculated). See Figures 2–6 for footnotes that give details on the drafting and retro-deformation of our five new cross sections (Deep Creek Range, Schell Creek and Duck Creek Ranges, Egan and Cherry Creek Ranges, Butte Mountains, and White Pine Range). Readers are referred to Long (2019) for details on the drafting and retro-deformation of the cross sections of the House Range, Confusion Range, Pancake Range, and Diamond Mountains, Fish Creek Range, and Mahogany Hills. The east-west overlap between the restored Deep Creek Range and Confusion Range cross sections and the restored Schell Creek and Duck Creek Ranges and Egan and Cherry Creek Range cross sections is the consequence of restoration of high-offset normal faults and the lines of section being located at different latitudes (Fig. 1). To view Figure 7 at full size, please visit https://doi.org/10.1130/GEOS.S.16984726 or access the full-text article on www.gsapubs.org.

3. CROSS-SECTION DRAFTING AND RETRO-DEFORMATION

3.1. Methods

In order to illustrate the pre-extensional deformation geometry across east-central Nevada and west-central Utah, we drafted and retro-deformed cross sections of five ranges between the latitudes of 39°20′N and 39°50′N (Figs. 2–6; lines of section are shown on Fig. 1; all cross sections are compiled on Fig. 7). The cross sections were constrained using published geologic mapping, including (from east to west), Rodgers (1987) for the Deep Creek Range; Gans et al. (1985) and Young (1960) for the Schell Creek and Duck Creek Ranges; Fritz (1968) for the Egan and Cherry Creek Ranges; Douglass (1960) for the Butte Range; and Humphrey (1960) for the White Pine Range. The lines of section for each cross section were chosen to maximize the number of across-strike exposures of the Paleogene subvolcanic unconformity, which is used as a reference datum for retro-deforming the tilting accommodated by normal faulting (e.g., Long, 2019). Stratigraphic thicknesses were determined from geometric constraints along the lines of section whenever possible. If thicknesses for rock units could not be determined along the line of section, then thicknesses listed on the published geologic maps or thicknesses shown on the isopach maps of Stewart (1980) were used. Stratigraphic units in each range were grouped together to the level of geologic periods, with a few exceptions (e.g., Lower Cambrian clastic units were separated from Middle-Upper Cambrian carbonate units; Ordovician and Silurian rocks were grouped together; and Pennsylvanian and Permian rocks were grouped together). The cross sections were drafted down to the lowest stratigraphic level exposed in each range.

Apparent dips of sedimentary bedding and flow or compaction foliation in volcanic rocks were projected onto the cross sections, and areas of similar apparent dip were divided into dip domains. Boundaries between adjacent dip domains were modeled as kink axes that bisect the interlimb angle (e.g., Suppe, 1983). Faults are shown as planar (unless geometric constraints on source mapping indicated otherwise), and their dip angles were determined, where possible, by the interaction of fault traces with topography. For faults that either were not precisely located, did not pass through sufficient topography, or could not be geometrically constrained using balancing constraints, we used an approximate modern dip angle of 60° (e.g., Anderson, 1951). Several of the older published geologic maps (most notably Young, 1960, in the Schell Creek and Duck Creek Ranges, and Fritz, 1968, in the Egan and Cherry Creek Ranges) interpreted faults with a present-day low dip angle that places younger stratigraphic units over older stratigraphic units as thrust faults. However, after the interpretations of several more recent studies that focus on extensional styles in Nevada (e.g., Proffett, 1977; Gans, 1982; Gans and Miller, 1983; Lund et al., 1993; Surpless et al., 2002; Long and Walker, 2015; Long, 2019), we have reinterpreted these faults either as highly rotated normal faults (e.g., for the Egan and Cherry Creek Ranges; Gans, 1982; Gans and Miller, 1983) or as normal faults with an original low dip angle (e.g., for the Schell Creek and Duck Creek Ranges; Gans et al., 1985).

In order to be retro-deformable, the cross sections were drafted to be internally consistent (i.e., with matching cutoff angles and consistent displacement magnitudes for all stratigraphic cutoffs offset by individual normal faults). In many places, the stratigraphic cutoffs necessary for matching contacts across normal faults have been eroded; in these cases, we drafted geometries that minimize fault offset. Each cross section was retro-deformed by restoring the offset on normal faults and untilting the Paleogene unconformity to horizontal (e.g., Long, 2019).

In addition to our five new cross sections, we utilized published cross sections of four ranges from Long (2019), including the House Range, Confusion Range, Pancake Range, and Diamond Mountains–Fish Creek Range (compiled on Fig. 7; lines of section shown on Fig. 1), which were drafted and retro-deformed by the same methods that we used in our study.

3.2. Results: Pre-Extensional Deformation Geometry from Cross-Section Retro-Deformation

The following section discusses (from east to west) the results of retro-deformation of our five new cross sections, as well as brief summaries of the pre-extensional geometry of the four published cross sections from Long (2019). In this section, "steeply dipping" is defined as ≥50°, "moderately dipping" indicates dips between 20° and 50°, and "shallowly dipping" is ≤20°.

3.2.1. House Range

Retro-deformation of the cross section of the House Range in Long (2019) defined a broad, gentle anticline, with shallowly dipping Cambrian sedimentary rocks exposed at the surface in both limbs (Fig. 7). The Paleogene subvolcanic unconformity lies within the Cambrian section, indicating that ~8 km of overlying Ordovician to Triassic sedimentary rocks had been eroded prior to the Paleogene. Neogene extension of 1.9 km (13%) was accommodated by steeply west- and east-dipping normal faults (Long, 2019). The anticline in the House Range represents the crest of the Sevier Culmination, a regional-scale, domal structural high interpreted to have formed above basement thrust sheets that were imbricated during the construction of the Sevier fold-thrust belt (e.g., Allmendinger et al., 1987; DeCelles and Coogan, 2006).

3.2.2. Confusion Range

Retro-deformation of the Confusion Range cross section in Long (2019) illustrates the geometry of east-vergent thrust faults and folds of the western Utah thrust belt (Greene, 2014), which accommodated ~10 km of shortening between the Late Jurassic and Eocene (Fig. 7). The Paleogene unconformity is subhorizontal and overlies shallowly west-dipping Devonian rocks in the eastern part of the range and folded Pennsylvanian–Permian rocks in the western

part. Moderate to steeply east- and west-dipping normal faults accommodated 1.8 km (7%) of Neogene extension in the Confusion Range (Long, 2019).

3.2.3. Deep Creek Range

The Deep Creek Range exposes an ~17-km-thick section of moderately west-dipping Neoproterozoic to Permian sedimentary rocks; this section is deformed by two generations of normal faults (Fig. 2) (Rodgers, 1987). The Paleogene subvolcanic unconformity is exposed on the western side of the range, where it dips ~35° west and is approximately disconformable with underlying Permian rocks. The older set of normal faults includes the Reilly Canyon fault, a shallowly east-dipping fault in the eastern part of the range with 16 km of top-down-to-east offset (which is interpreted as the primary structure responsible for westward tilting of the range), as well as three faults in the western part of the range that are interpreted as top-down-to-east faults that have been rotated to shallow westward dips (Rodgers, 1987). The younger set of normal faults consists of a series of closely spaced, shallowly east-dipping faults, each with ~0.5–1.5 km of offset. Retro-deformation of all normal faults and restoration of the Paleogene unconformity define 28.1 km of total extension (207%) (Fig. 2). The pre-extensional geometry defines the Water Canyon Anticline (Nelson, 1966; Rodgers, 1987), an overturned, west-vergent anticline with interlimb angles between 28° and 88° and an axial plane that steepens with structural depth. The asymmetry of the anticline suggests that it was likely constructed as a fault-propagation fold above a blind, west-vergent thrust fault (e.g., Suppe and Medwedeff, 1990). Construction of the anticline can be bracketed between Late Cretaceous (72.8 ± 0.2 Ma; $^{40}Ar/^{39}Ar$ hornblende age from a metamorphic aureole within Neoproterozoic–Cambrian rocks), pre-deformational metamorphism and intrusion of the undeformed late Eocene (39 ± 1 Ma; U-Pb zircon) Ibapah pluton (Rodgers, 1987), which is compatible with hinterland contractional deformation contemporaneous with shortening in the Sevier fold-thrust belt.

3.2.4. Schell Creek and Duck Creek Ranges

A 14-km-thick section of moderately west-dipping Neoproterozoic–Pennsylvanian sedimentary rocks is exposed in the Schell Creek and Duck Creek Ranges (Young, 1960) and has been deformed by two sets of normal faults (Fig. 3). The Paleogene unconformity is approximately disconformable with underlying Pennsylvanian rocks and is exposed on the western side of the Schell Creek Range, where it dips ~50° west, and on the western side of the Duck Creek Range, where it dips ~30° west. The older set of normal faults consists of a shallowly west-dipping system of closely spaced, low cutoff-angle (typically ~15°) faults that we call the Schell Creek Range detachment system. These faults consistently omit stratigraphy, cut stratigraphically downward toward the east, translate stratigraphic cutoffs eastward, and are interpreted as a system of genetically related, top-down-to-east normal faults that were active at shallow dip angles and were subsequently rotated to shallow westward dips (Fig. 3). The younger set of normal faults dips moderately eastward and includes the Duck Creek and Schell Creek faults (Young, 1960). These faults started out with steep eastward dips and were responsible for the significant westward tilting of the range (Gans et al., 1985) and the Schell Creek Range detachment system. Retro-deformation of all normal faults and restoration of the Paleogene unconformity define 36.3 km (221%) of total extension. Top-down-to-east offset on the Schell Creek Range detachment system accounted for 32.1 km of this total extension. The pre-extensional geometry, which is constrained by the disconformity between Paleogene volcanic rocks and underlying Pennsylvanian sedimentary rocks observed in both the Duck Creek and Schell Creek Ranges, defines an overall minimally deformed, subhorizontal Paleozoic section, with balancing constraints locally requiring open folds with amplitudes <1–2 km (Fig. 3). Projection of the Paleogene unconformity into the eastern part of the restored section is consistent with observations of Permian rocks underlying the unconformity to the east in the Northern Snake Range (Hose and Blake, 1976; Gans and Miller, 1983; Johnston, 2000).

3.2.5. Egan and Cherry Creek Ranges

The Egan and Cherry Creek Ranges contain an ~10-km-thick section of moderately west-dipping Neoproterozoic to Permian sedimentary rocks (Fritz, 1968); this section has been deformed by a system of east-dipping, top-down-to-east normal faults (Fig. 4). The Paleogene unconformity is exposed in the central and western Egan Range, where it disconformably overlies Pennsylvanian rocks and dips ~45° west. On the western flank of the Cherry Creek Range, the unconformity is approximately horizontal and overlies folded Pennsylvanian rocks. The Egan Range is deformed by a complex set of anastomosing, shallowly east-dipping normal faults, which originated as moderately to steeply east-dipping faults that were rotated domino-style during progressive extension (Fig. 4) (Gans, 1982; Gans and Miller, 1983). Normal faults in the Cherry Creek Range are closely spaced, dip moderately to the east, and are interpreted to represent originally high-angle normal faults that underwent a lesser degree of rotation than those in the Egan Range. Retro-deformation of all normal faults and restoration of the Paleogene unconformity indicate 15.8 km of extension (87%) and define a pre-extensional geometry dominated by subhorizontal to shallowly east-dipping Paleozoic rocks. On the western end of the Cherry Creek Range, open folds with amplitudes <1 km are interpreted to define the eastern edge of the Butte Synclinorium (Fig. 4), which is described below.

3.2.6. Butte Mountains

The Butte Mountains expose an ~3-km-thick section of folded Pennsylvanian to Triassic sedimentary rocks that have been deformed by moderately

east- and west-dipping, small-offset normal faults (Fig. 5) (Douglass, 1960). The Paleogene unconformity is exposed on the eastern side of the range where it dips ~5° east and overlies Permian and Triassic rocks. Retro-deformation defines 0.7 km of extension (3%) and reveals a series of upright, gentle folds superimposed within a broad, ~2-km-amplitude synclinal structural low called the Butte Synclinorium (Hose, 1977; Gans and Miller, 1983; Long, 2012, 2015).

3.2.7. White Pine Range

The White Pine Range contains an ~8-km-thick section of folded Cambrian to Permian sedimentary rocks that is deformed by west- and east-dipping, high-angle normal faults (Fig. 6) (Humphrey, 1960). The Paleogene unconformity is exposed on the eastern side of the range, where it overlies Pennsylvanian rocks and dips ~15° east. The oldest normal faults in the White Pine range are moderately east-dipping and have been deformed by a younger set of steeply west-dipping normal faults. Retro-deformation of fault offset and tilting of the Paleogene unconformity define 6.1 km of extension (30%). The pre-extensional geometry illustrates the open Illipah Anticline and the Little Antelope Syncline on its western flank (Humphrey, 1960; Long, 2015). The timing of folding is interpreted to predate intrusion of the Late Cretaceous (92.7 ± 2 Ma to 104.5 ± 4 Ma; K/Ar biotite; Putney, 1985) Monte Cristo and Seligman stocks on the western flank of Mount Hamilton; these stocks cut across small-scale thrust faults that are thought to be related to larger-scale folding in the range (Sonnevil, 1979).

3.2.8. Pancake Range

Retro-deformation of a cross section through the northern Pancake Range by Long (2019) defined an open syncline with Mississippian–Pennsylvanian rocks exposed in its hinge zone (Fig. 7). The Paleogene unconformity overlies shallowly west-dipping Mississippian rocks in the eastern part of the range and shallowly east-dipping Mississippian and Devonian rocks in the western part. Two steeply dipping normal faults accommodated a total of 0.4 km of extension (7%) (Long, 2019).

3.2.9. Diamond Mountains–Fish Creek Range–Mahogany Hills

Retro-deformation of a cross section through the Diamond Mountains, Fish Creek Range, and Mahogany Hills by Long (2019) illustrated the geometry of the Eureka Culmination, a 20-km-wide, open anticline interpreted as a fault-bend fold that structurally elevated Cambrian to Permian sedimentary rocks above an east-vergent, subsurface thrust fault (Long et al., 2014a) (Fig. 7). The timing of construction of the culmination is constrained by syn-contractional deposition of the ca. 114–99 Ma Newark Canyon Formation on its eastern limb (Long et al., 2014a; Di Fiori et al., 2020). The Paleogene unconformity in the Diamond Mountains and Fish Creek Range is subhorizontal and overlies complexly deformed Cambrian to Permian rocks. Two sets of high-angle normal faults predated the Paleogene unconformity, and their motion is bracketed between ca. 75 and ca. 60 Ma based on rapid cooling of their footwalls (Long et al., 2015). Retro-deformation of all normal faults defines 10.9 km (50%) of extension (Long, 2019). Readers are referred to Long et al. (2014a, 2015) for detailed descriptions of these structurally complex ranges.

4. PEAK TEMPERATURE DATA

4.1. Methods for RSCM Thermometry

Carbonaceous material originates from solid-state metamorphism of organic matter (e.g., Buseck and Huang, 1985) and is a common component of many metasedimentary rocks. The degree of structural organization of graphite within carbonaceous material is temperature-dependent and can be used as a quantitative geothermometer (e.g., Beyssac et al., 2002, 2003; Rahl et al., 2005; Lahfid et al., 2010; Kouketsu et al., 2014; Lünsdorf and Lünsdorf, 2016; Lünsdorf et al., 2017; McMillan and Golding, 2019). We utilized Raman spectroscopy of carbonaceous material (RSCM) thermometry (e.g., Beyssac et al., 2002, 2003; Rahl et al., 2005; Kouketsu et al., 2014) to measure the peak temperatures attained by 37 samples of sedimentary and metasedimentary rocks that we collected from six ranges in eastern Nevada and western Utah (Fig. 1; from east to west: the House Range, Deep Creek Range, Schell Creek Range, Egan Range, White Pine Range, and Fish Creek Range). Samples were collected from clastic and carbonate units that range in depositional age from Neoproterozoic to Pennsylvanian (Table 1). To sample younger stratigraphic levels, RSCM samples were collected within ~2 km north or south of the lines of section for all ranges except the House Range, where three samples were collected between ~20–25 km south of the line of section (Fig. 1). The locations of the RSCM samples were projected to their corresponding position on the cross sections of each range (Figs. 2–7). House Range samples that were collected farther away from the line of section were projected along strike to their same stratigraphic level on the cross section.

Measurements of carbonaceous material were performed on polished thin sections of each sample at the Eyring Materials Center at Arizona State University. Parameters, settings, and procedures used for the Raman spectrometer were identical to those of Long and Soignard (2016) (see Item S1 of the Supplemental Material[1] for additional details on methods). We collected data over the spectral range of 100–2000 cm^{-1}. Typically, between 12 and 14 individual grains of carbonaceous material were analyzed for each sample, in order to evaluate in-sample variation (with a total range between 8 and 17; Table 1). Carbonaceous material was generally present as ~5–25 μm patches (Fig. 8). A custom peak fitting program written by E. Soignard for Matlab (see Item S2 of the Supplemental Material[2] for additional details on this program) was used to determine peak positions, heights, widths, and areas

Supplementary material for: Late Cretaceous upper-crustal thermal structure of the Sevier hinterland: implications for the geodynamics of the Nevadaplano

Discussion 1: Analytical methods and supporting data for RSCM thermometry

Measurements of carbonaceous material were performed *in situ* on polished thin sections of each sample at the Eyring Materials Center at Arizona State University, using a Raman spectrometer custom-built by E. Soignard. Parameters, settings, and procedures used for the Raman spectrometer were identical to those of Long and Soignard (2016). The machine uses a 532 nm laser operated at a power of 3 mW. The laser was focused on carbonaceous material beneath transparent grains of quartz or calcite, in accordance with the procedures of Beyssac et al. (2003). Analyses were conducted on individual ~1 μm spots for 120 seconds over a spectral range of ~100-2,000 cm^{-1}. As many as 15-20 individual grains of carbonaceous material were analyzed from each sample in order to evaluate in-sample variation.

A custom peak fitting program written by E. Soignard for Matlab (also see Discussion 2 below) was used to determine the center positions, heights, widths (FWHM – full width at half maximum), shapes (the ratio of Gaussian to Lorentzian peak shape), and areas of up to five first-order Raman peaks (G, D1, D2, D3, and D4) between 1,000-1,800 cm^{-1} for each analyzed grain (Table S1). Peaks are identified visually and fit iteratively, with program-guided checks to ensure that peak locations are at a reasonable position. Any background slope is removed using a linear equation between 1,000-1,800 cm^{-1}. After fitting is complete, the program calculates parameters R1 and R2, which are the height and area ratios, respectively, defined by equations 1 and 2 of Rahl et al. (2005). Equation 3 of Rahl et al. (2005), which is calibrated to the R1 and R2 parameters, was used to calculate the peak temperature (T_{peak}) for analyses >400 °C. Equation 1 of Kouketsu et al. (2014), which is calibrated to the D1 FWHM, was used to calculate T_{peak} for analyses between 200–400 °C, and equation 2 of Kouketsu et al. (2014), which is calibrated to the D2 FWHM, was used to calculate T_{peak} for analyses <200 °C.

Supporting data for analyses from individual CM grains from each sample are shown on Table S1. The mean and standard deviation for R1, R2, D1 FWHM, D2 FWHM, and T_{peak} are reported on Table 1 in the main text. However, the calibration equation of Rahl et al. (2005) introduces an external uncertainty in T_{peak} of 50 °C, equation 1 of Kouketsu et al. (2014)

[1]Supplemental Material. Item S1 includes detailed methodology for RSCM and CAI analysis, supporting data for RSCM and CAI summary data, and instructions for using Matlab RSCM analysis program. Please visit https://doi.org/10.1130/GEOS.S.16417173 to access the supplemental material, and contact editing@geosociety.org with any questions.

[2]Supplemental Material. Item S2 includes Matlab peak fitting program file. See text footnote 1 for detailed instructions. Please visit https://doi.org/10.1130/GEOS.S.16417182 to access the supplemental material, and contact editing@geosociety.org with any questions.

TABLE 1. SUMMARY OF RAMAN SPECTROSCOPY OF CARBONACEOUS MATERIAL SAMPLES AND PEAK TEMPERATURE DETERMINATIONS

Sample	Latitude	Longitude	Structural depth below Paleogene unconformity (m)	Structural depth below top of Triassic section (m)	Depositional age	Map unit	Lithology	Temperature calibration	D1 FWHM		D2 FWHM		R1		R2		Peak temperature (°C)			n
									Mean	1σ	Mean	1σ	Mean	1σ	Mean	1σ	Mean	1σ	2 SE	
HR19-05	39° 00′ 57.8″	−113° 25' 18.5"	1800	−5400	Silurian	Laketown Dolomite	dolomite	Kouketsu et al. (2014) Equation 1	126	2	-	-	-	-	-	-	207	5	19	10
HR19-03	39° 02' 02"	−113° 20' 29.6"	500	−6800	Ordovician	Fillmore Formation	shale	Kouketsu et al. (2014) Equation 1	113	9	-	–	-	-	-	-	235	20	22	11
HR19-01	39° 03' 33.7"	−113° 15' 43.1"	50	−7250	Middle-Upper Cambrian	Notch Peak Formation	limestone	Kouketsu et al. (2014) Equation 1	98	4	-	-	-	-	-	-	267	8	19	11
HR19-13B	39° 13' 16.1"	−113° 22' 34.8"	−900	−8200	Middle-Upper Cambrian	Weeks Limestone	limestone	Rahl et al. (2005) Equation 3	-	-	-	-	0.616	0.144	0.418	0.049	457	23	32	12
HR19-12	39° 13' 48.2"	−113° 22' 36.3"	−1500	−8800	Middle-Upper Cambrian	Marjum Formation	limestone	Kouketsu et al. (2014) Equation 1	69	3	-	-	-	-	-	-	329	7	20	10
DCR17-20	39° 45' 49.1"	−114° 08' 11"	−900	−2950	Mississippian	Chainman Shale	limestone	Kouketsu et al. (2014) Equation 2	-	-	60	3	-	-	-	-	130	23	32	12
DCR17-17	39° 44' 42.1"	−114° 07' 29.5"	−2000	−4050	Devonian	Guilmette Formation	dolomite	Kouketsu et al. (2014) Equation 2	-	-	54	5	-	-	-	-	166	14	30	12
DCR17-15	39° 44' 09.3"	−114° 07' 09.9"	−3550	−5600	Ordovician–Silurian	Hanson Ck/Lone Mtn. Dolomite	dolomite	Kouketsu et al. (2014) Equation 1	84	4	-	-	-	-	-	-	298	8	17	13
DCR17-13	39° 44' 00.3"	−114° 05' 32.4"	−5050	−7100	Ordovician	Pogonip Group	limestone	Kouketsu et al. (2014) Equation 1	76	8	-	-	-	-	-	-	314	18	21	11
DCR17-11	39° 43' 56.3"	−114° 04' 53.7"	−5600	−7650	Middle-Upper Cambrian	undifferentiated limestone	limestone	Kouketsu et al. (2014) Equation 1	51	2	-	-	-	-	-	-	369	4	19	10
DCR17-09	39° 43' 42.4"	−114° 04' 16.3"	−5950	−8000	Middle-Upper Cambrian	undifferentiated limestone	limestone	Kouketsu et al. (2014) Equation 1	55	5	-	-	-	-	-	-	361	10	20	10
DCR17-07	39° 43' 54.5"	−114° 03' 43.8"	−6200	−8250	Middle-Upper Cambrian	undifferentiated limestone	limestone	Kouketsu et al. (2014) Equation 1	49	1	-	-	-	-	-	-	372	3	19	10
DCR17-03	39° 44' 06.2"	−114° 02' 32.6"	−7500	−9550	Lower Cambrian	Pioche Shale	slate	Kouketsu et al. (2014) Equation 1	45	1	-	-	-	-	-	-	381	3	13	13
DR-342J	39° 43' 40"	−113° 59' 55"	−9800	−11,850	Neoproterozoic	McCoy Creek Group, Unit e	slate/quartzite	Rahl et al. (2005) Equation 3	-	-	-	-	0.278	0.257	0.279	0.105	517	60	39	16
DR-329E	39° 45' 20"	−113° 53' 20"	−12,450	−14,500	Neoproterozoic	McCoy Creek Group, Unit b	graphitic argillite	Rahl et al. (2005) Equation 3	-	-	-	-	0.130	0.054	0.188	0.060	577	49	40	12
DR-338B	39° 44' 10"	−113° 54' 10"	−14,950	−17,000	Neoproterozoic	Trout Creek Formation, Unit 6	slate/quartzite	Rahl et al. (2005) Equation 3	-	-	-	-	0.144	0.077	0.188	0.071	581	53	44	11
DR-336A4	39° 43' 05"	−113° 53' 25"	−16,050	−18,100	Neoproterozoic	Trout Creek Formation, Unit 5	quartzite	Rahl et al. (2005) Equation 3	-	-	-	-	0.084	0.021	0.133	0.033	621	30	32	13
DR-334E	39° 45' 10"	−113° 53' 10"	−16,800	−18,850	Neoproterozoic	Trout Creek Formation, Unit 3	schist	Rahl et al. (2005) Equation 3	-	-	-	-	0.073	0.020	0.128	0.026	624	22	39	8
DR-433G	39° 44' 55"	−113° 52' 20"	−17,600	−19,650	Neoproterozoic	Trout Creek Formation, Unit 1	schist/quartzite	Rahl et al. (2005) Equation 3	-	-	-	-	0.106	0.059	0.162	0.071	597	59	43	13
SCR18-13	39° 28' 23"	−114° 38' 12"	−5000	−7700	Middle-Upper Cambrian	Windfall Formation	limestone	Kouketsu et al. (2014) Equation 1	93	4	-	-	-	-	-	-	278	8	20	10
SCR18-08	39° 28' 22"	−114° 36' 56"	−8500	−9950	Middle-Upper Cambrian	El Dorado Limestone	limestone	Kouketsu et al. (2014) Equation 1	65	4	-	-	-	-	-	-	338	9	19	11
SC16-06	39° 25' 29.8"	−114° 33' 39.3"	−11,100	−12,750	Neoproterozoic	McCoy Creek Group, Unit c	slate/siltstone	Rahl et al. (2005) Equation 3	-	-	-	-	0.322	0.100	0.337	0.054	472	32	36	11
SC16-05	39° 25' 27"	−114° 33' 11.7"	−11,800	−13,450	Neoproterozoic	McCoy Creek Group, Unit e	slate/quartzite	Rahl et al. (2005) Equation 3	-	-	-	-	0.224	0.113	0.275	0.075	511	51	35	17
SC16-04	39° 25' 38.3"	−114° 32' 36.6"	−12,550	−14,200	Neoproterozoic	McCoy Creek Group, Unit g	graphitic phyllite	Rahl et al. (2005) Equation 3	-	-	-	-	0.195	0.061	0.267	0.053	512	42	35	14
SC16-03	39° 25' 45.4"	−114° 32' 24.8"	−13,150	−14,800	Neoproterozoic	McCoy Creek Group, Unit i	marble	Rahl et al. (2005) Equation 3	-	-	-	-	0.174	0.061	0.267	0.070	505	58	40	15
SC16-01	39° 25' 56.1"	−114° 31' 58.9"	−13,950	−15,600	Neoproterozoic	McCoy Creek Group, Unit k	marble	Rahl et al. (2005) Equation 3	-	-	-	-	0.160	0.067	0.247	0.071	523	57	38	16
ER19-13	39° 44' 14.3"	−114° 55' 37.8"	−3000	−5650	Devonian	Sevy Dolomite	dolomite	Kouketsu et al. (2014) Equation 2	-	-	56	3	-	-	-	-	154	18	19	13
ER19-18	39° 43' 38.4"	−114° 54' 39.1"	−6150	−8800	Middle-Upper Cambrian	Windfall Formation	limestone	Kouketsu et al. (2014) Equation 1	114	4	-	-	-	-	-	-	233	8	19	11
ER19-11	39° 44' 03.6"	−114° 51' 37.5"	−7950	−10,600	Lower Cambrian	Pioche Shale	shale	Kouketsu et al. (2014) Equation 1	80	1	-	-	-	-	-	-	307	3	18	11
MH19-06	39° 15' 06.4"	−115° 29' 30"	−2650	−5450	Devonian	Nevada Limestone	limestone	Kouketsu et al. (2014) Equation 2	-	-	60	3	-	-	-	-	126	20	34	10
MH16-04	39° 14' 01.3"	−115° 32' 20.4"	−5250	−8050	Ordovician	Goodwin Formation	limestone	Kouketsu et al. (2014) Equation 2	-	-	53	2	-	-	-	-	174	14	30	12
MH16-02	39° 14' 03.6"	−115° 32' 47"	−5650	−8450	Middle-Upper Cambrian	Secret Canyon Shale	shale	Rahl et al. (2005) Equation 3	-	-	-	-	0.273	0.070	0.319	0.050	478	35	33	14
MH16-01	39° 14' 00.1"	−115° 34' 03.1"	−6550	−9350	Middle-Upper Cambrian	Geddes Limestone	limestone	Rahl et al. (2005) Equation 3	-	-	-	-	0.101	0.036	0.166	0.044	591	37	36	12
FCR17-07	39° 27' 19.9"	−115° 58' 13.8"	250	−7000	Ordovician	Goodwin Formation	limestone	Kouketsu et al. (2014) Equation 2	-	-	59	1	-	-	-	-	134	8	32	10
FCR17-04	39° 27' 17.1"	−115° 59' 03.9"	−100	−7350	Middle-Upper Cambrian	Secret Canyon Formation	limestone	Kouketsu et al. (2014) Equation 2	-	-	57	3	-	-	-	-	146	22	35	10
FCR17-01	39° 25' 48.1"	−115° 59' 22.1"	−750	−8000	Middle-Upper Cambrian	El Dorado Limestone	dolomite	Kouketsu et al. (2014) Equation 1	96	3	-	-	-	-	-	-	271	6	18	12
FCR17-09	39° 26' 53.4"	−115° 59' 54.3"	−1300	−8800	Lower Cambrian	Pioche Shale	limestone	Kouketsu et al. (2014) Equation 2	-	-	56	4	-	-	-	-	153	27	34	11

Note: Peak temperatures >400 °C were determined using Equation 3 of Rahl et al. (2005), peak temperatures between 200–400 °C were determined using Equation 1 of Kouketsu et al. (2014), and peak temperatures <200 °C were determined using Equation 2 of Kouketsu et al. (2014). R1 and R2 parameters were calculated using the procedures of Rahl et al. (2005), and D1 FWHM (full width at half maximum) and D2 FWHM values were calculated using the procedures of Kouketsu et al. (2014). Internal variability in R1, R2, D1 FWHM, D2 FWHM, and peak temperature is indicated by 1σ uncertainty. Peak temperature is also reported with 2 standard errors (SE), calculated after Cooper et al. (2013), from quadratic addition of 1σ internal error and external error of ±50 °C from the Rahl et al. (2005) calibration, ±30 °C from the Kouketsu et al. (2014) calibration (equation 1), or ±50 °C from the Kouketsu et al. (2014) calibration (equation 2), divided by the square root of the number of analyses (n). All structural and stratigraphic depth measurements are rounded to the nearest 50 m.

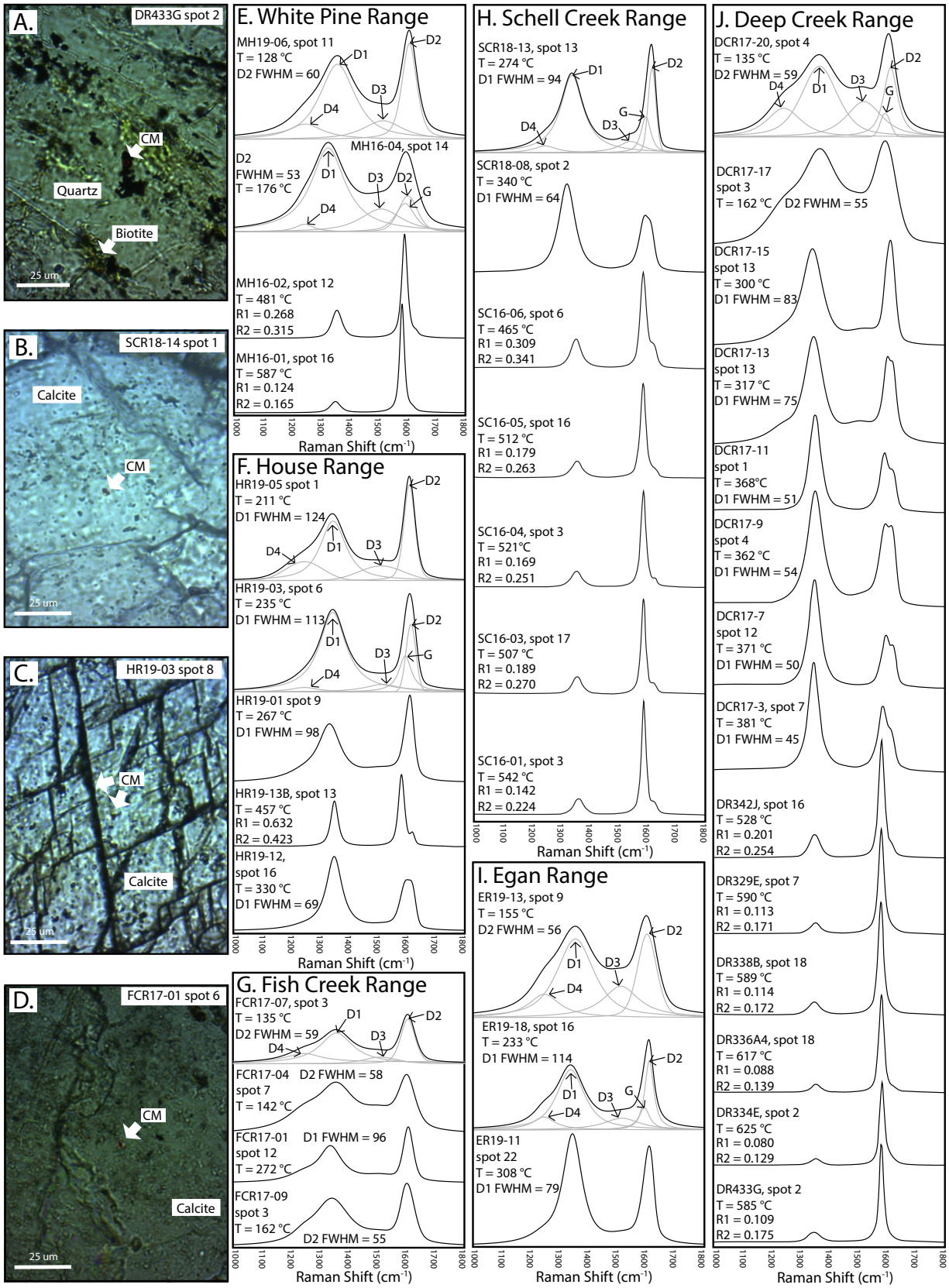

Figure 8. (A–D) Photomicrographs of representative examples of individual analyzed grains of carbonaceous material (CM) (plane polarized light). (E–J) Representative examples of individual Raman spectra from each of the 37 analyzed Raman spectroscopy of carbonaceous material (RSCM) samples. Spectra from each range are shown in stratigraphic order, with peak temperatures (T), R1 and R2 values calculated after Rahl et al. (2005), and D1 full width at half maximum (FWHM) or D2 FWHM calculated after Kouketsu et al. (2014). The individual shapes of the graphite peak (G) and defect peaks (D1, D2, D3, and D4) are shown for the top 1–2 spectra in each range.

for Raman spectra of each analyzed grain. To quantify peak temperatures, we utilized the procedures of Rahl et al. (2005) and Kouketsu et al. (2014); these procedures involve fitting as many as five Raman peaks (G, D1, D2, D3, and D4) in the wave number range of 1000–1800 cm^{-1}. Peak temperatures above 400 °C were determined using Equation 3 of Rahl et al. (2005), which is calibrated to the height ratio of D1/G (their parameter R1) and the area ratio of D1/(G + D1 + D2) (their parameter R2). Peak temperatures below 400 °C were determined using Equations 1 and 2 of Kouketsu et al. (2014), which are calibrated to the full width at half maximum (FWHM) of D1 (for temperatures of 200–400 °C; their Equation 1) or D2 (for temperatures of 150–200 °C; their Equation 2).

Representative examples of individual Raman spectra from each sample are shown on Figure 8, and a summary of peak temperature determinations for each sample is shown in Table 1 (see Item S1 of the Supplemental Material [footnote 1] for data from individual analyses). The peak temperature reported for each sample is the mean of all measured grains, and each temperature is reported at a 2-sigma standard error level, which accounts for internal uncertainty from our measurements and the external uncertainty from the calibrations of Rahl et al. (2005) and Kouketsu et al. (2014) (see footnote of Table 1).

4.2. Methods for Compilation of Published CAI Data

The RSCM thermometers that we used are calibrated most accurately for rocks that achieved peak temperatures higher than ~100–150 °C (Rahl et al., 2005; Kouketsu et al., 2014), and therefore this technique is best utilized for rocks that have been deeply buried or heated. In order to provide semiquantitative constraints on peak temperature conditions achieved within the uppermost ~3–5 km of the crust, and to compare to the RSCM temperatures obtained from our shallowest samples, we compiled published conodont alteration index (CAI) data for Cambrian through Triassic sedimentary rocks from all nine of our studied ranges. The CAI is based on the progressive change in color that occurs as conodonts are heated (e.g., Epstein et al., 1977) and has been utilized extensively as a semiquantitative estimate of peak temperature achieved during burial and metamorphism. While CAI temperature determinations are subject to diagenetic processes, quantitative color determination bias, and complex thermal histories of individual conodonts that may cause disagreement between CAI and RSCM temperature estimates (e.g., McMillan and Golding, 2019, Golding and McMillan, 2020), these complexities are typically the most significant for higher temperature determinations (≥~100–200 °C). Therefore, the CAI data that we compile are likely the most representative of peak thermal conditions at the shallowest crustal levels. CAI values are ranked on a scale of 1–6, with corresponding peak temperatures of <50–80 °C (CAI of 1), <50–90 °C (CAI of 1.5), 60–140 °C (CAI of 2), 110–200 °C (CAI of 3), 190–300 °C (CAI of 4), 300–480 °C (CAI of 5), and 360–550 °C (CAI of 6) (Epstein et al., 1977; Königshof, 2003).

For each of our nine studied ranges, we compiled published CAI values for samples collected within a 50 km radius of our lines of section. CAI values were compiled from Crafford (2007) for ranges in Nevada and from Harris et al. (1980) for ranges in Utah. These two studies provide a robust, spatially and stratigraphically distributed data set of temperature ranges, which are particularly important for the shallowest stratigraphic levels where we lack RSCM data along our transect. For each range, CAI values of all rock samples from each geologic period were grouped together, and representative CAI values were determined by calculating a mode that captured ≥66% of the compiled data for each geologic period in each range (supporting data and additional details on methods are shown in Item S1 of the Supplemental Material [footnote 1]). If a CAI mode that accounts for ≥66% of datapoints could not be determined for a given period, then the range of CAI values that satisfied the ≥66% requirement was used as an alternative. A summary of our representative CAI values (or ranges of CAI values) from each range is shown in Table 2. Representative CAI ranges are graphed on Figures 9 and 10 with vertical error bars that correspond to the top and bottom of rocks in that period and horizontal error bars that correspond to the lower and upper limits of the temperature scale of Königshof (2003).

4.3. Results: Temperature-Depth Relationships in Each Range

Here, we integrate our RSCM thermometry and CAI compilation with pre-extensional depths from our retro-deformed cross sections, in order to quantify paleo-peak thermal field gradients for the upper crust of the Sevier hinterland. Temperature versus depth relationships for each range are discussed below from east to west and are supported by Figures 9 and 10.

In order to estimate maximum and minimum thermal field gradients for each range, two types of sample depths were calculated: structural depths below the Paleogene unconformity and structural depths below the reconstructed top of the Triassic section. Semi-continuous deposition of sedimentary rocks continued until the Triassic across eastern Nevada and western Utah (e.g., Stewart and Poole, 1974; Stewart, 1980), and sections of Triassic rocks up to ~900 m thick have been documented proximal to our cross sections (Stewart, 1980). Sedimentary rocks of interpreted Early Jurassic age are only preserved in one locality in northeastern Nevada, ~60 km north of our Egan and Cherry Creek Ranges cross section (Stewart and Carlson, 1978; Stewart, 1980). Early Cretaceous sedimentary rocks are only preserved at the longitude of the Diamond Mountains and Fish Creek Ranges and are interpreted to have been deposited proximal to active structures of the Central Nevada thrust belt (Long et al., 2014a, 2014b; Di Fiori et al., 2020). Therefore, though it is possible that Jurassic and Cretaceous sedimentary rocks were locally deposited in areas of the Sevier hinterland, their lack of preservation, combined with our CAI compilation (Table 2) that shows that Mississippian–Pennsylvanian rocks that were buried as deep as ~3–4 km below the top of the Triassic section often yield CAI values of 1–1.5 (<50–90 °C), precludes deep burial under

TABLE 2. SUMMARY OF DOMINANT CAI VALUES FROM EACH RANGE, DIVIDED OUT BY PERIOD

Range	Period	CAI (mode)	Temperature range	n[1]	Period thickness m[2]
House Range	Triassic	CAI = 1–1.5	<50–90 °C	n = 3/3	750
	Pennsylvanian–Permian	CAI = 1–1.5	<50–90 °C	n = 3/4	2100
	Mississippian	CAI = 1.5–2	50–140 °C	n = 8/9	950
	Devonian	CAI = 1.5–2	50–140 °C	n = 4/5	1450
	Ordovician–Silurian	CAI = 3	110–200 °C	n = 5/7	1850
Confusion Range	Triassic	CAI = 1–1.5	<50–90 °C	n = 3/3	600
	Pennsylvanian–Permian	CAI = 1–1.5	<50–90 °C	n = 5/6	2600
	Mississippian	CAI = 2	60–140 °C	n = 8/10	800
	Devonian	CAI = 2	60–140 °C	n = 6/6	1800
	Ordovician–Silurian	CAI = 3–4	110–300 °C	n = 10/11	1600
Deep Creek Range	Triassic	CAI = 1–1.5	<50–90 °C	n = 3/3	900
	Pennsylvanian–Permian	CAI = 1–2	<50–140 °C	n = 12/19	1850
	Mississippian	CAI = 1–2	<50–140 °C	n = 8/11	550
	Devonian	CAI = 2–3	60–200 °C	n = 5/6	1500
	Ordovician–Silurian	CAI = 4–5	190–480 °C	n = 6/10	1850
Schell Creek and Duck Creek Ranges	Triassic	CAI = 1	<50–80 °C	n = 2/2	900
	Pennsylvanian–Permian	CAI = 1–1.5	<50–90 °C	n = 11/15	2250
	Mississippian	CAI = 1–2	<50–140 °C	n = 3/4	500
	Devonian	CAI = 3	110–200 °C	n = 4/5	1500
	Ordovician–Silurian	CAI = 3	110–200 °C	n = 7/8	1950
	Middle-Upper Cambrian	CAI = 4	190–300 °C	n = 6/6	2650
Egan and Cherry Creek Ranges	Triassic	CAI = 1	<50–80 °C	n = 3/3	900
	Pennsylvanian–Permian	CAI = 1–1.5	<50–90 °C	n = 17/21	2600
	Mississippian	CAI = 1.5–2	50–140 °C	n = 2/2	900
	Devonian	CAI = 3–4	110–300 °C	n = 3/5	1650
	Ordovician–Silurian	CAI = 3	110–200 °C	n = 7/8	2100
	Middle-Upper Cambrian	CAI = 4	190–300 °C	n = 6/7	1950
Butte Range	Triassic	CAI = 1	<50–80 °C	n = 2/2	900
	Pennsylvanian–Permian	CAI = 1	<50–80 °C	n = 14/17	2800
	Mississippian	CAI = 1–2	<50–90 °C	n = 9/14	2000
	Devonian	CAI = 2–5	60–480 °C	n = 12/15	900
	Ordovician–Silurian	CAI = 3	110 - 200 °C	n = 7/8	2900
	Middle-Upper Cambrian	CAI = 4	190–300 °C	n = 6/7	1900
White Pine Range	Triassic	CAI = 1	<50–80 °C	n = 2/2	900
	Pennsylvanian–Permian	CAI = 1	<50–80 °C	n = 14/15	2800
	Mississippian	CAI = 1–1.5	<50–90 °C	n = 17/25	1200
	Devonian	CAI = 1–1.5	<50–90 °C	n = 51/69	700
	Ordovician–Silurian	CAI = 4–6	190–550 °C	n = 34/46	2450
	Middle-Upper Cambrian	CAI = 3	110–200 °C	n = 1/1	1850
Pancake Range	Triassic	CAI = 1	<50–80 °C	n = 3/3	900
	Pennsylvanian–Permian	CAI = 1	<50–80 °C	n = 9/10	2000
	Mississippian	CAI = 1–1.5	<50–90 °C	n = 25/33	1400
	Devonian	CAI = 1–1.5	<50–90 °C	n = 56/66	1000
	Ordovician–Silurian	CAI = 3–6	110–550 °C	n = 31/48	2050
Fish Creek Range	Triassic	CAI = 1	<50–80 °C	n = 3/3	900
	Pennsylvanian–Permian	CAI = 1–2	<50–140 °C	n = 21/22	1250
	Mississippian	CAI = 1–1.5	<50–90 °C	n = 23/34	1900
	Devonian	CAI = 1–1.5	<50–90 °C	n = 54/81	1450
	Ordovician–Silurian	CAI = 1–4	50–300 °C	n = 60/86	1800
	Middle-Upper Cambrian	CAI = 3	110–200 °C	n = 2/2	1650

[1]n is displayed as the number of conodont alteration index (CAI) data points that meet the ≥66% mode requirement over the total number of data points collected. See Supplemental Material (text footnote 1) for complete CAI data compilation.
[2]Thickness rounded to the nearest 50 m.

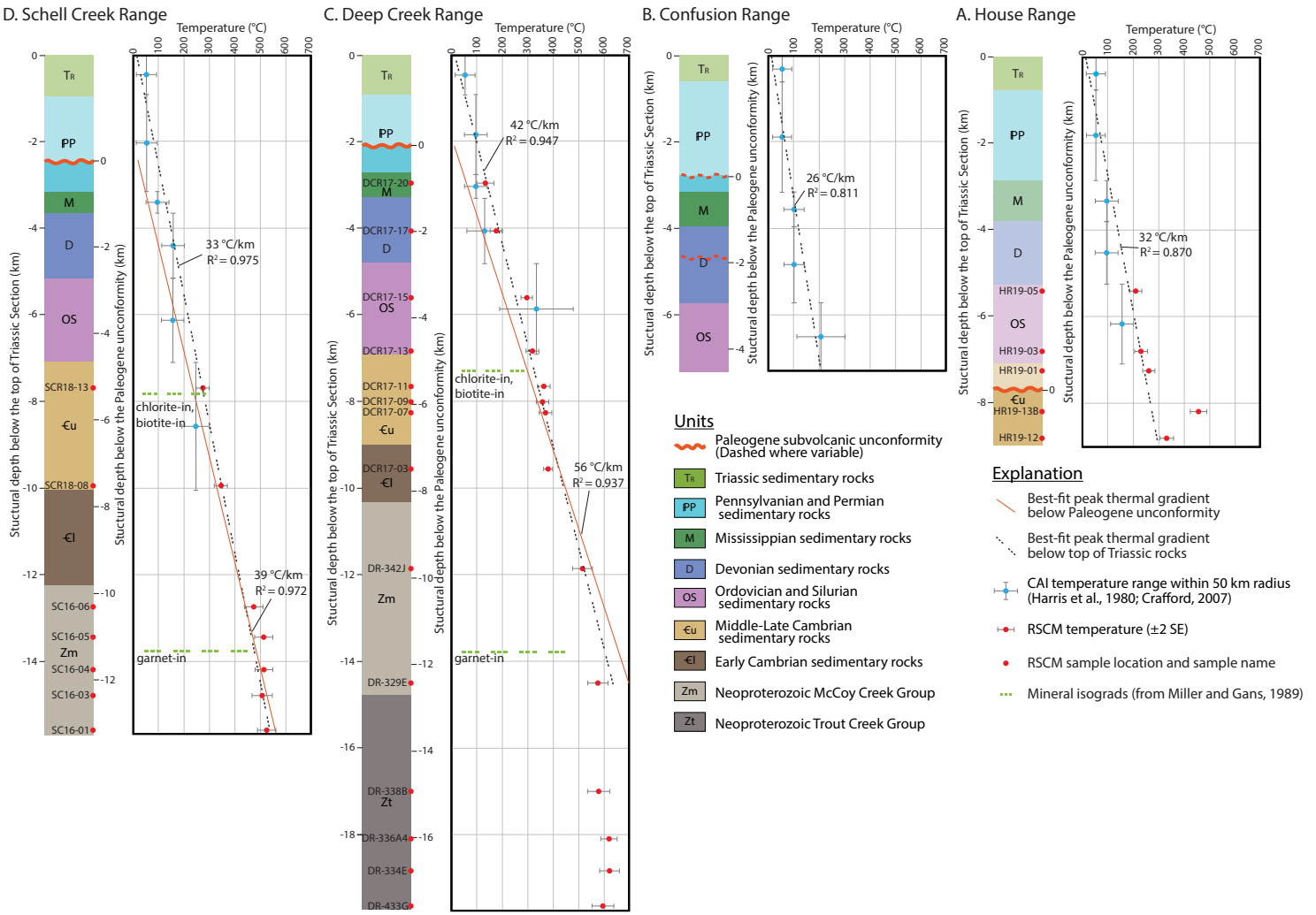

Figure 9. Temperature versus depth graphs plotting Raman spectroscopy of carbonaceous material (RSCM) and compiled conodont alteration index (CAI) peak temperatures for the: (A) House Range; (B) Confusion Range (lower and upper stratigraphic range of the Paleogene unconformity is shown); (C) Deep Creek Range; and (D) Schell Creek Range (ranges are organized from east on the right to west on the left). Columns to the left of each graph depict structural thicknesses for each period determined from the cross sections (Fig. 7). Translucent areas represent rocks that were eroded prior to deposition of volcanic rocks above the Paleogene unconformity. Structural depths are measured from the top of the Triassic section (left-hand side of columns) and below the Paleogene unconformity (right-hand side of columns).

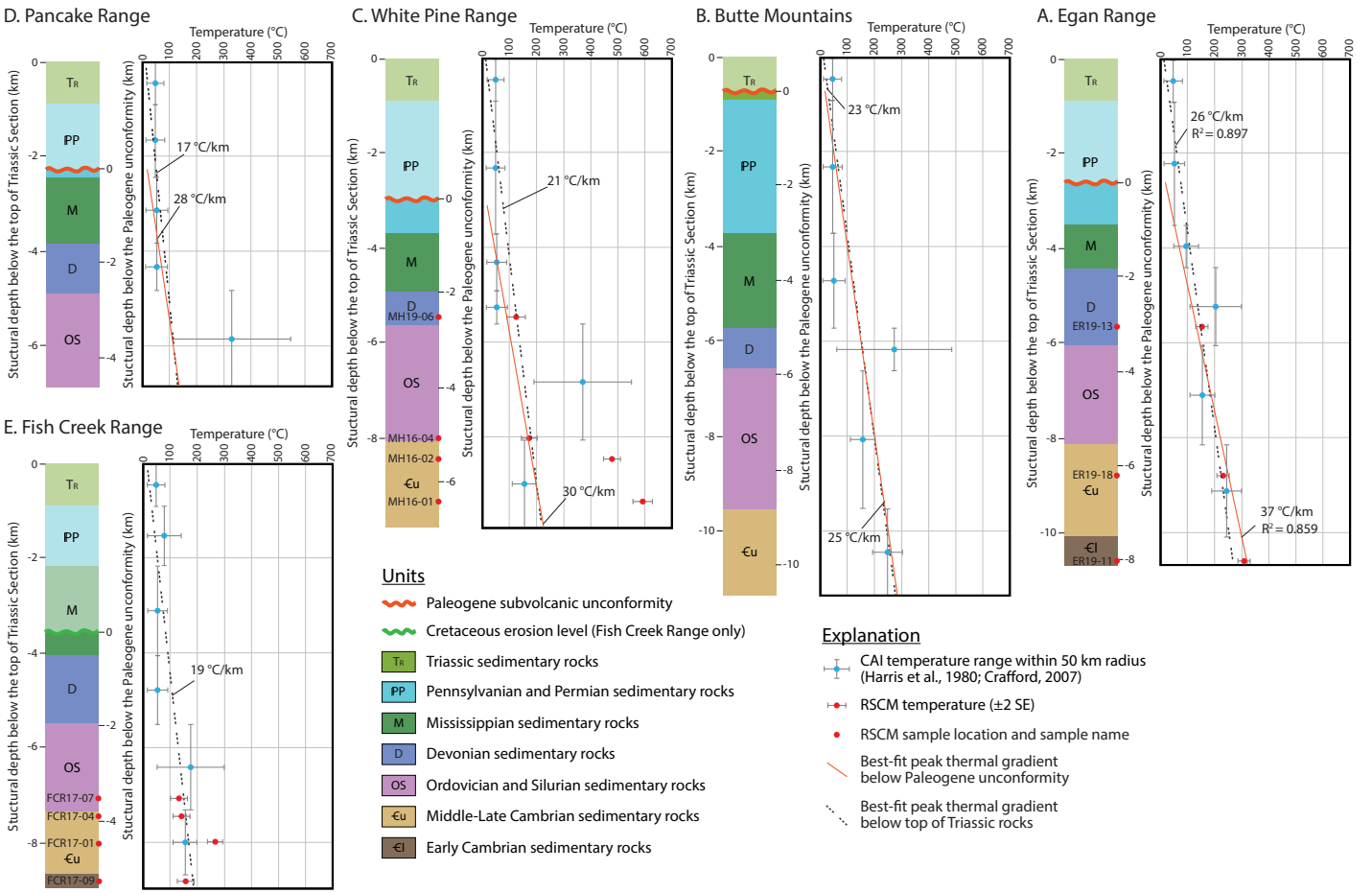

Figure 10. Temperature versus depth graphs plotting Raman spectroscopy of carbonaceous material (RSCM) and compiled conodont alteration index (CAI) peak temperatures for the: (A) Egan Range; (B) Butte Mountains; (C) White Pine Range; (D) Pancake Range; and (E) Fish Creek Range (ranges are organized from east on the right to west on the left). Columns to the left of each graph depict structural thicknesses for each period determined from the cross sections (Fig. 7). Translucent areas represent rocks that were eroded prior to deposition of volcanic rocks above the Paleogene unconformity. Structural depths are measured from the top of the Triassic section (left-hand side of columns) and below the Paleogene unconformity (right-hand side of columns).

a thick, regionally continuous Jurassic–Cretaceous sedimentary section (e.g., Long, 2012). Therefore, we interpret that the structural depth below the top of the Triassic section represents the maximum depth attained by our samples.

The Paleogene unconformity records the stratigraphic position of the surface of the Sevier hinterland during the late Eocene–Oligocene Great Basin ignimbrite flare-up, which predates the onset of upper-crustal normal faulting on eight of our nine cross sections (e.g., Long, 2019; the Fish Creek Range did experience pre-volcanic extension; this unique case is discussed below). Therefore, the structural depth below the Paleogene unconformity represents the minimum depth of our samples prior to extension-related exhumation.

In six of the nine studied ranges (Deep Creek, Schell Creek, Egan, Butte, White Pine, and Pancake Ranges), the Paleogene unconformity lies within Pennsylvanian or higher stratigraphic levels, defining minimal (~1–3 km) erosion, which can be bracketed to have occurred between the Triassic and the

Paleogene. In most of these ranges, two best-fit lines were fit through all temperature data (and were forced to pass through a temperature of 15 ± 10 °C at 0 depth, in order to replicate a realistic surface temperature range) and are interpreted to represent the respective maximum (using depths below the Paleogene unconformity) and minimum (using depths below the top of the Triassic section) peak thermal field gradients. In contrast, the House Range and Confusion Range both record up to ~5–8 km of erosion associated with Cretaceous structural uplift of the Sevier Culmination (Allmendinger et al., 1987; DeCelles and Coogan, 2006; Greene, 2014), and the Fish Creek Range records up to ~8 km of extension-related exhumation that predates the Paleogene unconformity (Long et al., 2015). For these ranges, only best-fit lines below the top of the Triassic section were calculated.

4.3.1. House Range

RSCM temperatures from five Cambrian–Silurian samples from the House Range decrease upward from ~329 °C to ~207 °C, with one outlier of ~455 °C (Fig. 9A). CAI temperatures decrease upsection from 110 to 200 °C in Ordovician–Silurian rocks, to 50–140 °C in Devonian–Mississippian rocks, to <50–90 °C in Pennsylvanian–Triassic rocks. Using structural depths below the top of the Triassic section, all temperature data (with the exception of the anomalously hot Cambrian sample) are best-fit down to 8.8 km by a thermal gradient of 32 °C/km. This gradient must have been attained prior to the ~8 km of erosion accommodated during the ca. 110–88 Ma (DeCelles and Coogan, 2006) construction of the Sevier Culmination. The anomalously high peak temperature recorded by a Cambrian sample is interpreted as the likely result of localized heating, perhaps from a proximal igneous intrusion associated with the Jurassic Notch Peak pluton, which is mapped ~4 km to the south of the line of section (Fig. 7).

4.3.2. Confusion Range

CAI temperatures from the Confusion Range decrease upward from 110 to 300 °C in Ordovician rocks, to 60–140 °C in Devonian–Mississippian rocks, to <50–90 °C in Pennsylvanian–Triassic rocks (Fig. 9B). Utilizing structural depths below the top of the Triassic section, similar to our approach for the House Range, yields a best-fit gradient of 26 °C/km down to a 7.4 km paleo-depth.

4.3.3. Deep Creek Range

RSCM temperatures from the lowest five Deep Creek Range samples, which lie between 17.6 and 12.5 km below the Paleogene unconformity, overlap within error between ~625 °C and ~575 °C (Fig. 9C). Moving upward, temperatures decrease from ~575 °C to ~130 °C between 12.5 and 0.9 km depths (n = 10). CAI values decrease upsection from 190 to 480 °C in Ordovician–Silurian rocks, to 60–200 °C in Devonian rocks, to 50–140 °C in Mississippian–Permian rocks, to <50–90 °C in Triassic rocks. RSCM and CAI data in the Deep Creek Range define an approximately linear pattern down to a depth of 12.5 km below the Paleogene unconformity (14.5 km below the top of the Triassic section) and are best-fit by minimum and maximum gradients of 42 °C/km and 56 °C/km (Fig. 9C). Below 12.5 km depth, temperatures are approximately constant, with an average of ~600 °C.

4.3.4. Schell Creek Range

RSCM temperatures from the lowest four Schell Creek Range samples, which span from 13.9 to 11.8 km below the Paleogene unconformity, overlap within error between ~525 °C and ~505 °C (Fig. 9D). Moving upward, RSCM temperatures decrease from ~505 °C to ~280 °C between 11.8 and 5.0 km depths (n = 4). CAI values decrease upward from 190 to 300 °C in Middle-Upper Cambrian rocks, to 110–200 °C in Ordovician–Devonian rocks, to 50–140 °C in Mississippian rocks, to <50–90 °C in Pennsylvanian–Triassic rocks. The CAI and RSCM data define an approximately linear pattern with depth that is best-fit by minimum and maximum gradients of 33 °C/km and 39 °C/km (Fig. 9D).

4.3.5. Egan Range

RSCM samples from the Egan Range (n = 3) yielded ~305 °C at a depth of 8.0 km below the Paleogene unconformity, ~235 °C at 6.2 km, and ~155 °C at 3.0 km (Fig. 10A). CAI values generally decrease upward, from 190 to 300 °C in Middle-Upper Cambrian rocks, to 110–200 °C in Ordovician–Silurian rocks, 110–300 °C in Devonian rocks, to 50–140 °C in Mississippian rocks, to <50–90 °C in Pennsylvanian–Triassic rocks. These data are best-fit by minimum and maximum gradients of 26 °C/km and 37 °C/km (Fig. 10A).

4.3.6. Butte Mountains

CAI temperatures for the Butte Mountains generally decrease upward, from 190 to 300 °C in Middle-Upper Cambrian rocks, to 110–200 °C in Ordovician–Silurian rocks, to a broad range of 60–480 °C in Devonian rocks, to <50–90 °C in Mississippian–Triassic rocks (Fig. 10B). The data are fit by minimum and maximum gradients of 23 °C/km and 25 °C/km (Fig. 10B), which pass through the lower end of the CAI error range for Devonian rocks.

4.3.7. White Pine Range

Samples from the White Pine Range (n = 4) yielded RSCM temperatures of ~590 °C at ~6.6 km below the Paleogene unconformity, ~480 °C at ~5.7 km,

~175 °C at ~5.3 km, and ~125 °C at ~2.7 km (Fig. 10C). CAI values decrease upward from 110 to 200 °C in Cambrian rocks to <50–90 °C in Devonian to Triassic rocks, with the exception of a 190–550 °C temperature range for Ordovician–Silurian rocks. Collectively, the temperature data from the White Pine Range are not internally consistent and do not increase linearly with depth. The anomalously high RSCM temperatures from the lowest two samples may be the result of localized heating associated with Cretaceous granite stocks at Mount Hamilton (e.g., Putney, 1985); these stocks are mapped within 1–2 km of these samples (Fig. 6). The origin of the 190–550 °C range in CAI temperatures for Ordovician–Silurian rocks is more difficult to interpret and is broad enough to prevent constraining a meaningful thermal gradient. Excluding the two anomalously high RSCM temperatures and the large CAI range from Ordovician–Silurian rocks, the remaining data are best-fit to a depth of 9.3 km by minimum and maximum gradients of 21 °C/km and 30 °C/km (Fig. 10C). Alternatively, it would require minimum and maximum gradients of 58 °C/km and 82 °C/km to achieve the temperatures attained by the lowest two RSCM samples. Based on the results from adjacent ranges, we consider it more likely that 21–30 °C/km is a representative estimate for the peak thermal gradient through the White Pine Range, and that the lowest two RSCM samples experienced localized heating associated with the Cretaceous intrusions.

4.3.8. Pancake Range

CAI temperatures for the region surrounding the Pancake Range are between 110 and 550 °C for Ordovician–Silurian rocks and decrease abruptly moving upward, from <50–90 °C in Devonian–Mississippian rocks, to <50–80 °C in Pennsylvanian–Triassic rocks (Fig. 10D). The overlap in CAI temperatures between Devonian–Triassic rocks combined with the large CAI temperature range for Ordovician–Silurian rocks is prohibitive for calculating a precise thermal gradient. We calculate a minimum gradient of 17 °C/km and a maximum gradient of 28 °C/km, which both pass through the low end of the CAI temperature range for Ordovician–Silurian rocks (Fig. 10D).

4.3.9. Fish Creek Range

RSCM temperatures from Fish Creek Range samples (n = 4) yield peak temperatures of ~155 °C at 8.8 km, ~145 °C at 7.4 km, and ~135 °C at 7.0 km below the top of the Triassic section, with one outlier of ~270 °C at 8.0 km (Fig. 10E). CAI temperatures generally decrease upsection, from 110 to 200 °C in Cambrian rocks, to 50–300 °C in Ordovician–Silurian rocks, to <50–90 °C in Devonian–Mississippian rocks, to <50–140 °C in Pennsylvanian–Permian rocks, to <50–80 °C in Triassic rocks. Because the Fish Creek Range experienced a history of Early Cretaceous (ca. 115–100 Ma) uplift and erosion during construction of the Eureka Culmination (Long et al., 2014a; Di Fiori et al., 2020), followed by normal fault-related exhumation between ca. 75–60 Ma (Long et al., 2015), we did not use depth below the Paleogene unconformity to constrain the thermal gradient. Instead, we used depths below the top of the Triassic section. We estimate a post-Triassic, pre-Early Cretaceous thermal gradient of 19 °C/km, which excludes the anomalously high-temperature RSCM sample (the best-fit gradient increases to 22 °C/km, if this sample is included).

5. DISCUSSION

5.1. Implications for the Thermal History and Geodynamics of the Nevadaplano

Here, we interpret the significance of the temperature-depth relationships yielded by our nine studied ranges for the thermal history of the Sevier hinterland plateau, by placing them in the context of published geochronology and interpretations for Cordilleran magmatism and metamorphism in this region. This discussion is supported by Figure 11, which shows contoured isotherms from our temperature data sets.

On the eastern end of our transect, the House and Confusion Ranges yielded peak, post-Triassic thermal field gradients of 29 ± 3 °C/km, which must have been attained prior to the 110–88 Ma construction of the Sevier Culmination. Moving westward, average thermal gradients increase to 49 ± 7 °C/km in the Deep Creek Range, 36 ± 3 °C/km in the Schell Creek Range, and 32 ± 6 °C/km in the Egan Range (Figs. 9 and 11). Previous workers (most notably Miller and Gans, 1989) have presented evidence for a Late Cretaceous tectonothermal episode that affected the Sevier hinterland crust in westernmost Utah and eastern Nevada. Supporting evidence comes from the Deep Creek, Snake, Schell Creek, and Egan Ranges, which contain exposures of Neoproterozoic–Lower Cambrian sedimentary rocks that record greenschist-facies (chlorite-biotite grade) to amphibolite-facies (garnet-grade) metamorphism that is interpreted to have been contemporaneous with Late Cretaceous granitic magmatism (e.g., Rodgers, 1987; Miller et al., 1988; Miller and Gans, 1989). These Neoproterozoic–Lower Cambrian sedimentary rocks (with the exception of rocks in the Northern Snake Range, which are discussed below) were interpreted to restore to pre-extensional depths of ~8–14 km and exhibit mineral assemblages that bracket an approximate peak temperature range between 300 °C and 650 °C, defining field gradients locally as high as ~50 °C/km (Miller et al., 1988; Miller and Gans, 1989).

The timing of attainment of peak temperatures in easternmost Nevada is interpreted to be contemporaneous with Late Cretaceous regional granitic magmatism, dated at ca. 75 Ma in the Kern Mountains (U-Pb zircon; Lee et al., 1986), ca. 80–86 Ma in the Southern Snake Range (K-Ar muscovite; Lee et al., 1970, 1980, 1986), and ca. 70–100 Ma in the Northern Snake Range (U-Pb zircon and $^{147}Sm/^{144}Nd$ monazite; Lee and Fischer, 1985; U-Pb zircon; Miller et al., 1988; $^{147}Sm/^{144}Nd$, $^{176}Lu/^{177}Hf$ garnet and U-Th-Pb zircon; Cooper et al., 2010; U-Pb zircon; Gottlieb, 2017), and is also bracketed by post-metamorphic cooling dated at ca. 61–90 Ma in the Schell Creek Range (K-Ar

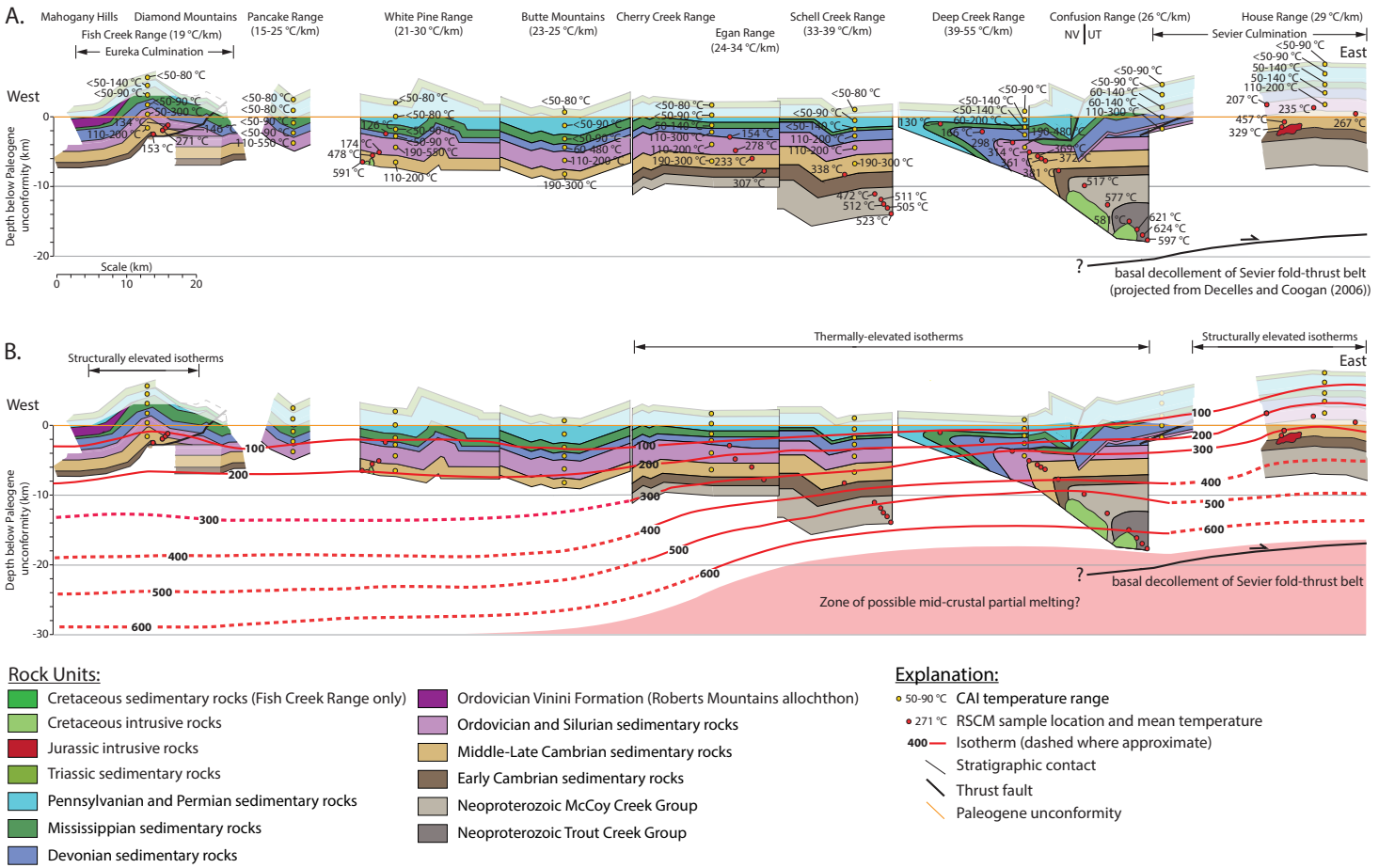

Figure 11. (A) Simplified, smaller-scale version of the cross-section compilation from Figure 7B, plotting the Raman spectroscopy of carbonaceous material (RSCM) samples and associated temperatures (shown without errors for simplicity) and conodont alteration index (CAI) temperature ranges for rocks of each period from each range. CAI data points were placed where period thickness is most representative, typically in the middle of the cross sections or in proximity to RSCM samples. The basal décollement of the Sevier fold-thrust belt from DeCelles and Coogan (2006; their Fig. 8F) is projected below the House and Confusion Ranges, after Long (2019). (B) Version of the master cross section in A with approximate contoured isotherms, which were determined from CAI and RSCM temperature values and from downward projection of calculated thermal field gradients (Figs. 9 and 10). Localized heating adjacent to small (~0.5 km² map area; Humphrey, 1960) Cretaceous granite intrusions on the western end of the White Pine Range (Fig. 6) is not contoured.

and $^{40}Ar/^{39}Ar$ muscovite; Lee et al., 1980; Miller et al., 1988), ca. 73 Ma in the Deep Creek Range ($^{40}Ar/^{39}Ar$ hornblende; Rodgers, 1987), and ca. 75–78 Ma in the Northern Snake Range (U-Pb monazite and $^{40}Ar/^{39}Ar$ hornblende; Lee et al., 1981; Lee et al., 1987). Therefore, after Miller et al. (1988), Miller and Gans (1989), and Barton (1990), we interpret that the peak thermal conditions recorded in the Deep Creek, Schell Creek, and Egan Ranges were likely attained during the Late Cretaceous (ca. 70–90 Ma, and perhaps locally as early as ca. 100 Ma).

On the western end of our transect, post-Triassic thermal gradients in the Butte, White Pine, Pancake, and Fish Creek Ranges typically vary between ~20–30 °C/km. The ~20–30 °C/ km gradients from the westernmost four ranges are similar to the 29 ± 3 °C/km gradients from the House and Confusion Ranges, which implies that this represents an approximate "background" post-Triassic peak thermal gradient range for the Sevier hinterland, which contrasts with the elevated thermal gradients in easternmost Nevada.

The spatial correlation between Late Cretaceous magmatism and metamorphism in the region surrounding the Deep Creek, Schell Creek, and Egan Ranges and the elevated thermal gradients obtained in this study indicate that granitic magmatism was likely a primary mechanism for upward heat transport (e.g., Barton et al., 1988; Miller and Gans, 1989; Long and Soignard, 2016). Based on peraluminous compositions that imply minimal mantle contribution, most studies agree that these Late Cretaceous granites represent the upward rise of melts generated during an episode of lower-crustal anatexis (e.g., Barton, 1987; Barton, 1990; Miller and Gans, 1989; Wells and Hoisch, 2008; Gottlieb, 2017). Competing hypotheses for the genesis of Late Cretaceous anatexis include an influx of magma and heat following delamination of mantle lithosphere (Wells and Hoisch, 2008; Wells et al., 2012) or an eastward migration of subduction-related magmatism in combination with relaxation of isotherms within recently thickened crust (Miller and Gans, 1989). The elevated thermal gradients that we document are best explained by a mechanism that would focus heating below the Deep Creek, Schell Creek, and Egan Ranges. We argue that crustal thickening alone is likely not enough to explain the observed spatial pattern of heating, as crustal thicknesses were not greatest below these three ranges but instead are interpreted to have been approximately uniform between the Fish Creek Range and the House Range during the final stages of shortening in the Late Cretaceous–early Paleogene (~55–65 km; Chapman et al., 2015; Long, 2019). Thermal anomalies associated with crustal thickening, as well as any radiogenic heat that accumulated during this process, would be predicted to be broadly distributed over the region of thickened crust (Chen et al., 2019); however, the amount and even presence of heating associated with crustal thickening is debated, with some numerical simulations indicating that thickening leads to cooling rather than heating (Huerta et al., 1998; Babeyko et al., 2002).

Instead, after Wells and Hoisch (2008) and Wells et al. (2012), we interpret that delamination of the lithospheric mantle centered beneath the Deep Creek, Schell Creek, and Egan Ranges provides an intriguing possible explanation for the Late Cretaceous magmatism, metamorphism, and elevated thermal field gradients observed in these three ranges. We acknowledge that crustal thickening and associated conductive relaxation of isotherms may aid in the development of mantle drips and subsequent mantle delamination (Schott and Schmeling, 1998; Morency and Doin, 2004), and therefore that crustal thickening in eastern Nevada likely promoted delamination of mantle lithosphere. Furthermore, thickening and softening of the mantle lithosphere promote development of a lithospheric root and can be achieved by ductile strain (e.g., Molnar et al., 1998; Conrad and Molnar, 1999; Conrad, 2000), such as that proposed by strain compatibility and mass-balance considerations in the Sevier hinterland (Oldow et al., 1989, 1990; Wells and Hoisch, 2008). Lithospheric delamination can also be invoked to explain the presence of high peak thermal gradients in the absence of mapped granite intrusions (Wells and Hoisch, 2008), which is what we document in the Schell Creek Range (Fig. 11B).

Geodynamic models indicate that mantle delamination can occur at small spatial scales (~100 km wide) (Schott and Schmeling, 1998; Morency and Doin, 2004), which is corroborated by seismic imaging of an interpreted ~100-km-wide lithospheric drip below the Sierra Nevada batholith in southeastern California, which is expressed at the surface as an area of anomalous topography ~120 km wide (Saleeby and Foster, 2004). Our retro-deformed cross section (Figs. 7 and 11) defines a pre-extensional width of 74 km from the western edge of the Egan and Cherry Creek Ranges to the eastern edge of the Deep Creek Range, which is on the same approximate order as modeled and interpreted widths for small-scale mantle delamination (e.g., Schott and Schmeling, 1998; Morency and Doin, 2004; Saleeby and Foster, 2004; West et al., 2009). Furthermore, models of lithospheric delamination suggest that this process can initiate and sustain upper-crustal magmatism for several tens of millions of years (e.g., Bird, 1979; Houseman et al., 1981; England and Houseman, 1989; Kay and Kay, 1991, 1993; Wells and Hoisch, 2008; Ducea, 2011; Yao et al., 2012; Ducea et al., 2013), which is on the same order as the duration of lower-crustal anatexis proposed for eastern Nevada (e.g., Miller et al., 1988; Miller and Gans, 1989; Barton, 1990).

The elevated thermal field gradients that we document in easternmost Nevada, combined with high upper-crustal field gradients documented along strike, including ~60 °C/km in the Grant Range (~170 km to the south-southwest of our Egan Range cross section) (Long and Soignard, 2016) and ~40–60 °C/km in the Pequop Mountains (~150 km to the north of our Egan Range cross section) (Zuza et al., 2020a) imply that Cretaceous upper-crustal heating may have been distributed over an extensive region of the Sevier hinterland. This has implications for significant thermal weakening of the middle-upper crust, including elevating the ~250–275 °C quartz crystal-plastic transition (e.g., Stipp et al., 2002) to depths as shallow as ~5 km, and for the ~650–700 °C minimum temperatures necessary to initiate partial melting of pelitic rocks (e.g., Spear et al., 1999) possibly being attained at depths as shallow as ~18–20 km (Fig. 11B). The significant strength reduction that likely accompanied middle-lower crustal melting (e.g., Rosenberg and Handy, 2005) may have helped drive additional lithospheric delamination (e.g., Morency and Doin, 2004).

5.2. Comparison to Interpreted Metamorphic History of the Northern Snake Range

Our studied ranges all contain sedimentary rocks that restore to pre-extensional paleo-depths of ≤20 km (Figs. 7 and 11). However, based on thermobarometry data, Neoproterozoic–Lower Cambrian metasedimentary rocks in the footwall of the Northern Snake Range décollement (NSRD) (Fig. 1) are interpreted to have experienced peak metamorphic conditions of ~6–8 kbar (equivalent to burial to ~23–30 km peak depths, assuming a lithostatic gradient of ~0.26 kbar/km) and ~500–650 °C (Lewis et al., 1999; Cooper et al., 2010). These peak depths place these Neoproterozoic–Lower Cambrian rocks at ~2–3 times their original stratigraphic depths, which has been reconciled with interpretations of significant structural burial contemporaneous with shortening in the Sevier fold-thrust belt, including burial under east-vergent thrust sheets (which requires at least ~90 km of top-to-east displacement; Bartley and Wernicke, 1984) or burial via west-vergent back-thrusting (which requires at least ~30 km of thrust offset to have been fed to the surface in easternmost Nevada; Lewis et al., 1999).

Several aspects of these interpreted structural models are not in agreement with our temperature-depth data sets. First, on our reconstructed cross sections, we do not see evidence for high-offset thrust faults breaching surface levels in the Sevier hinterland in easternmost Nevada, and instead, we document low-magnitude shortening accommodated by folding (Fig. 7; also discussed in more detail below), which has also been documented by Armstrong (1972), Gans and Miller (1983), and Long (2015, 2019). Second, our compiled CAI data from Mississippian–Triassic rocks within and in the regions surrounding our studied ranges indicate consistently low temperatures (always ≤140 °C for Mississippian–Permian rocks, and always ≤90 °C for Triassic rocks; Table 2; Figs. 9 and 10), which precludes deep burial under thick, surface-breaching thrust sheets. Third, the pressure-temperature (P-T) conditions from the footwall of the NSRD obtained by Cooper et al. (2010) correspond to a peak thermal field gradient range of 17–28 °C/km down to ~23–30 km depths, which is significantly lower (by a factor of ~1.5–3) than the peak thermal gradients that we document in the adjacent Schell Creek and Deep Creek Ranges. We document similar peak temperatures to those obtained in the footwall of the NSRD at much shallower paleo-depths; for example, ~60 km along-strike to the north in the Deep Creek Range, we obtained ~500–625 °C peak temperatures at paleo-depths of 12–20 km, and ~40 km to the west in the Schell Creek Range, we obtained ~500–525 °C peak temperatures at 13–16 km paleo-depths. Also, based on downward projection of the elevated thermal gradients in these two ranges, any pelitic rocks in easternmost Nevada that were buried to ~23–30 km depths would be predicted to have attained peak temperatures >700 °C (Fig. 11B), and therefore to have undergone partial melting (e.g., Spear et al., 1999). However, partial melting has not been described in any of the rocks in the NSRD footwall (e.g., Miller et al., 1983; Cooper et al., 2010; Lee et al., 2017).

The lack of evidence for large-offset structures that could have accommodated deep structural burial in the region surrounding the Northern Snake Range, combined with the high thermal field gradients that we obtain from adjacent ranges, further highlights the long-standing debate fueled by the disagreements between pressure estimates in Sevier hinterland core complexes and regional field relationships (e.g., Gans and Miller, 1983; Miller et al., 1983; Lee et al., 1987; Thorman et al., 1991; Hodges and Walker, 1992; Camilleri and Chamberlain, 1997; Lewis et al., 1999; McGrew et al., 2000; Cooper et al., 2010; Henry et al., 2011; Long, 2012; Hallett and Spear, 2014, 2015; Zuza et al., 2020a, 2020b). One possibility for reconciling these disparate observations is that tectonic overpressure (e.g., Petrini and Podladchikov, 2000; Schmalholz and Podladchikov, 2013; Gerya, 2015; Hoiland, 2019) potentially affected the rocks in the Northern Snake Range, as was recently suggested for the Ruby–East Humboldt–Wood Hills–Pequop Mountains core complex in northeastern Nevada by Zuza et al. (2020a, 2020b).

5.3. Implications for the Magnitude and Style of Extensional and Contractional Deformation

Though ancillary to the main goals of this paper, our retro-deformed cross sections provide information about the style and magnitude of Cordilleran shortening and Cenozoic extension across eastern Nevada and western Utah. Here, we summarize extension and shortening magnitudes from our five new cross sections through the Deep Creek, Schell Creek–Duck Creek, Egan–Cherry Creek, Butte, and White Pine Ranges.

Extension magnitudes are greatest in the Deep Creek and Schell Creek–Duck Creek Ranges, which yielded 207% and 221% extension, respectively (Fig. 7 and Table 3). The Egan and Cherry Creek Ranges yielded 87% extension, the Butte Mountains 3%, and the White Pine Range 30%. The present-day width between the eastern edge of the Deep Creek Range and the western edge of the White Pine Range (as measured on Fig. 7A) is 170.6 km. After restoring the widths of valleys using the methods described above (e.g., Long, 2019) and accounting for east-west overlap between the restored Schell Creek and Duck Creek Ranges and Egan and Cherry Creek Ranges cross sections, the total pre-extensional width between the Deep Creek Range and the White Pine Range (as measured on Fig. 7B) is 97.2 ± 4.6 km. Therefore, our reconstruction defines 73.4 ± 4.6 km of total extension (76 ± 8%). This is similar to the 78.4 ± 25.3 km extension value obtained between the Northern Snake Range and the White Pine Range by Long (2019), which had a larger error range due to uncertainty regarding restoration of displacement on the NSRD. Integrating our total extension estimate with the present-day average crustal thickness of 32 ± 1 km at this latitude (Gilbert, 2012), and assuming that the lower crust was homogeneously extended by the same magnitude as the upper crust, restoration of extension defines an average pre-extensional crustal thickness of 56 ± 4 km. This should be considered a maximum thickness estimate, since it doesn't account for potential magmatic underplating at the base of the crust during the Paleogene Great Basin ignimbrite flare-up (e.g., Gans, 1987).

Our five new cross sections, when combined with the Pancake Range cross section of Long (2019), span the width of the Eastern Nevada Fold Belt

TABLE 3. ESTIMATES OF EXTENSION AND SHORTENING FROM OUR FIVE NEW CROSS SECTIONS

Range or Basin	Present-day length (km)	Pre-extensional length (km)	Extension (km)	Extension (%)
Deep Creek Range	41.7	13.6	28.1	207
Spring Valley	24.3	7.7 ± 1.2	16.6 ± 1.2	214 ± 7
Schell Creek and Duck Creek Ranges	56.9[1]	16.4	36.3	221
Steptoe Valley	7.2	2.9 ± 3.1	4.3 ± 3.1	148 ± 73
Egan and Cherry Creek Ranges	34.0	18.2	15.8	87
Butte Valley	1.2	0.8 ± 0.3	0.4 ± 0.3	45 ± 42
Butte Mountains	22.7	22.0	0.7	3
White Pine Range	26.3	20.2	6.1	30
Total (measured from Fig. 7)	170.6	97.2 ± 4.6	73.4 ± 4.6	76 ± 8

Range or Basin	Miss.–Penn. contact line length (km)[2]	Miss.–Penn. contact east-west length (km)[2]	Shortening (km)	Shortening (%)
Deep Creek Range	41.8	32.2	9.6	23
Schell Creek and Duck Creek Ranges	50.0	48.5	1.5	3
Egan and Cherry Creek Ranges	21.7	21.2	0.5	2
Butte Mountains	23.1	22.0	1.1	5
White Pine Range	21.6	20.2	1.4	6
Pancake Range	6.9	6.1	0.8	12

[1]Due to the geometry of extension in the Schell Creek and Duck Creek Ranges, an amount equal to the extension magnitude has been added to the present-day length. Readers are referred to the footnotes in text Figures 3 for a detailed description of extension calculations in the Schell Creek Range.

[2]Line lengths were measured from using the Mississippian–Pennsylvanian (Miss.–Penn.) contact, which is most frequently exposed at the Paleogene erosion surface. Shortening estimates were not attempted in basins due to lack of exposure.

of Long (2015) (Fig. 1). The retro-deformed cross sections define open folds with amplitudes up to 1–2 km, including the Butte Synclinorium and Illipah Anticline (Fig. 7). In the Deep Creek Range, the overturned, west-vergent Water Canyon Anticline (Rodgers, 1987) is the only tight fold observed. Shortening was measured on cross sections of individual ranges by measuring the line length of the stratigraphic contact between Mississippian and Pennsylvanian rocks, which was the closest contact to the Paleogene erosion surface on all six cross sections, and comparing this line length with the pre-extensional east-west cross section length. In the Deep Creek Range, the Water Canyon Anticline accommodated at least 9.6 km (23%) of shortening. To the west, shortening is 1.5 km (3%) in the Schell Creek and Duck Creek Ranges, 0.5 km (2%) in the Egan and Cherry Creek Ranges, 1.1 km (5%) in the Butte Mountains, 1.4 km (6%) in the White Pine Range, and 0.8 km (12%) in the Pancake Range. This corresponds to a cumulative estimate of 14.9 km of shortening (12%) accommodated within the Eastern Nevada fold belt at our studied latitude. Therefore, Cordilleran structural provinces of the Sevier hinterland, including (from west to east; Fig. 1) the Central Nevada Thrust Belt (~10–15 km shortening; Taylor et al., 1993, 2000; Long et al., 2014a, 2014b), the Eastern Nevada Fold Belt (~15 km shortening; this study), and Western Utah Thrust Belt (~10 km shortening; Greene, 2014) accommodated ~35–40 km of cumulative shortening at this latitude. The minimal shortening in the Sevier hinterland, when combined with the ~56 km crustal thickness attained by the end of Cordilleran shortening (this study), provides support for the interpretation of Long (2019) that westward underthrusting of thick, unrifted North American continental crust under eastern Nevada (a kinematic requirement of the ~220 km of shortening measured in the Sevier fold-thrust belt at this latitude by DeCelles and Coogan, 2006) was the primary mechanism of crustal thickening in this portion of the hinterland, and therefore was of first-order importance for construction of the high-elevation Nevadaplano.

6. CONCLUSIONS

(1) Temperature-depth relationships define post-Triassic peak thermal field gradients of 29 ± 3 °C/km in two ranges in westernmost Utah, elevated gradients in three ranges in easternmost Nevada (from east to west: 49 ± 7 °C/km, 36 ± 3 °C/km, and 32 ± 6 °C/km), and typical gradients between ~20–30 °C/km in four ranges in east-central Nevada. The

elevated thermal field gradients in easternmost Nevada are interpreted to have been attained during Late Cretaceous (ca. 70–90 Ma) regional granitic magmatism and shallow-crustal metamorphism.

(2) Our data are compatible with published interpretations of Late Cretaceous lithospheric mantle delamination under the Sevier hinterland, which triggered lower-crustal anatexis and the resulting rise of granitic melts into the middle-upper crust. We interpret that granite emplacement was the primary source of upward heat transport in easternmost Nevada. Heating likely resulted in significant thermal weakening of the middle crust, including yielding temperatures high enough to generate partial melting at depths as shallow as ~18 km.

(3) The lack of evidence for high-offset thrust faults in easternmost Nevada that could have accommodated deep structural burial of rocks in the footwall of the Northern Snake Range core complex, combined with peak thermal gradients that we document in adjacent ranges that are 1.5–3 times as high as those implied by thermobarometry in the Northern Snake Range, further highlights the long-standing debate over reconciling pressure estimates with field relationships in Cordilleran core complexes, and allows for the possibility of tectonic overpressure.

(4) Retro-deformation of cross sections defines 73.4 ± 4.6 km of extension (76 ± 8%) across eastern Nevada, which restores to a pre-extensional crustal thickness of 56 ± 4 km. We document ~15 km of shortening across the Eastern Nevada fold belt, which when combined with published estimates from adjacent thrust belts, defines modest (~35–40 km) shortening across the Sevier hinterland at this latitude. The minimal hinterland shortening combined with ~56-km-thick crust supports the interpretation that underthrusting of thick, unrifted North American crust beneath eastern Nevada was the primary thickening mechanism that constructed the Nevadaplano.

ACKNOWLEDGMENTS

We would like to thank Jesslyn Starnes for her assistance in RSCM data collection and Quinn Zunino for his help collecting samples in eastern Nevada, as well as helping to navigate the Nevada mountains. This study was supported by start-up funds from the Washington State University School of the Environment awarded to S. Long and grants from the Geological Society of America and the Nevada Petroleum Geological Society awarded to N. Blackford.

REFERENCES CITED

Allmendinger, R.W., 1992, Fold and thrust tectonics of the western United States exclusive of the accreted terranes, *in* Burchfiel, B.C., Lipman, P.W., and Zoback, M.L., eds., The Cordilleran Orogen: Conterminous U.S.: Boulder, Colorado, Geological Society of America, The Geology of North America, v. G-3, https://doi.org/10.1130/DNAG-GNA-G3.583.

Allmendinger, R.W., Hauge, T.A., Hauser, E.C., Potter, C.J., Klemperer, S.L., Nelson, K.D., Knuepfer, P., and Oliver, J., 1987, Overview of the COCORP 40°N transect, western United States: The fabric of an orogenic belt: Geological Society of America Bulletin, v. 98, p. 308–319, https://doi.org/10.1130/0016-7606(1987)98<308:OOTCNT>2.0.CO;2.

Anderson, E.M., 1951, The Dynamics of Faulting and Dyke Formation with Application to Britain: Edinburgh, UK, Oliver and Boyd, 206 p.

Armstrong, R.L., 1972, Low-angle (denudation) faults, hinterland of the Sevier orogenic belt, eastern Nevada and western Utah: Geological Society of America Bulletin, v. 83, no. 6, p. 1729–-1754, https://doi.org/10.1130/0016-7606(1972)83[1729:LDFHOT]2.0.CO;2.

Atwater, T., 1970, Implications of plate tectonics for the Cenozoic tectonic evolution of western North America: Geological Society of America Bulletin, v. 81, no. 12, p. 3513–3536, https://doi.org/10.1130/0016-7606(1970)81[3513:IOPTFT]2.0.CO;2.

Babeyko, A.Y., Sobolev, S.V., Trumbull, R.B., Oncken, O., and Lavier, L.L., 2002, Numerical models of crustal scale convection and partial melting beneath the Altiplano-Puna plateau: Earth and Planetary Science Letters, v. 199, no. 3–4, p. 373–388, https://doi.org/10.1016/S0012-821X(02)00597-6.

Bartley, J.M., and Wernicke, B.P., 1984, The Snake Range Décollement interpreted as a major extensional shear zone: Tectonics, v. 3, no. 6, p. 647–657, https://doi.org/10.1029/TC003i006p00647.

Barton, M., Battles, D., Debout, G., Capo, R., Christensen, J., Davies, S., Hanson, R., Michelsen, C., and Trim, H., 1988, Mesozoic contact metamorphism in the western United States, *in* Ernst, W.G., Metamorphism and Crustal Evolution of the Western United States: Rubey Volume VII: Englewood Cliffs, New Jersey, Prentice Hall, p. 111–178.

Barton, M.D., 1987, Lithophile-element mineralization associated with Late Cretaceous two- mica granites in the Great Basin (USA): Geology, v. 15, p. 337–340, https://doi.org/10.1130/0091-7613(1987)15<337:LMAWLC>2.0.CO;2.

Barton, M.D., 1990, Cretaceous magmatism, metamorphism, and metallogeny in the east-central Great Basin, *in* Anderson, J.L., ed., The Nature and Origin of Cordilleran Magmatism: Geological Society of America Memoir 174, p. 283–302, https://doi.org/10.1130/MEM174-p283.

Beaumont, C., Jamieson, R.A., Nguyen, M.H., and Lee, B., 2001, Himalayan tectonics explained by extrusion of a low-viscosity crustal channel coupled to focused surface denudation: Nature, v. 414, p. 738–742, https://doi.org/10.1038/414738a.

Best, M.G., Barr, D.L., Christiansen, E.H., Gromme, S., Deino, A.L., and Tingey, D.G., 2009, The Great Basin Altiplano during the middle Cenozoic ignimbrite flare-up: Insights from volcanic rocks, *in* Rise and Fall of the Nevadaplano—Part 1: International Geology Review, v. 51, no. 7–8, https://doi.org/10.1080/00206810902867690.

Beyssac, O., Goffé, B., Chopin, C., and Rouzaud, J.N., 2002, Raman spectra of carbonaceous material in metasediments: A new geothermometer: Journal of Metamorphic Geology, v. 20, p. 859–871, https://doi.org/10.1046/j.1525-1314.2002.00408.x.

Beyssac, O., Goffé, B., Petitet, J.P., Froigneux, E., Moreau, M., and Rouzaud, J.N., 2003, On the characterization of disordered and heterogeneous carbonaceous materials by Raman spectroscopy: Spectrochimica Acta. Part A: Molecular and Biomolecular Spectroscopy, v. 59, p. 2267–2276, https://doi.org/10.1016/S1386-1425(03)00070-2.

Bird, P., 1979, Continental Delamination and the Colorado Plateau: Journal of Geophysical Research, v. 84, p. 7561–7571, https://doi.org/10.1029/JB084iB13p07561.

Burchfiel, B.C., Cowan, D.S., and Davis, G.A., 1992, Tectonic overview of the Cordilleran orogen in the western United States, *in* Burchfiel, B.C., Lipman, P.W., and Zoback, M.L., eds., The Cordilleran Orogen: Conterminous U.S.: Boulder, Colorado, Geological Society of America, The Geology of North America, v. G-3, p. 407–480, https://doi.org/10.1130/DNAG-GNA-G3.407.

Buseck, P.R., and Huang, B.J., 1985, Conversion of carbonaceous material to graphite during metamorphism: Geochimica et Cosmochimica Acta, v. 49, no. 10, p. 2003–2016, https://doi.org/10.1016/0016-7037(85)90059-6.

Camilleri, P.A., and Chamberlain, K.R., 1997, Mesozoic tectonics and metamorphism in the Pequop Mountains and Wood Hills region, northeast Nevada: Implications for the architecture and evolution of the Sevier orogen: Geological Society of America Bulletin, v. 109, no. 1, p. 74–94, https://doi.org/10.1130/0016-7606(1997)109<0074:MTAMIT>2.3.CO;2.

Cassel, E.J., Breecker, D.O., Henry, C.D., Larson, T.E., and Stockli, D.F., 2014, Profile of a paleoorogen: High topography across the present-day Basin and Range from 40 to 23 Ma: Geology, v. 42, no. 11, p. 1007–1010, https://doi.org/10.1130/G35924.1.

Chapman, J.B., Ducea, M.N., DeCelles, P.G., and Profeta, L., 2015, Tracking changes in crustal thickness during orogenic evolution with Sr/Y: An example from the North American Cordillera: Geology, v. 43, no. 10, p. 919–922, https://doi.org/10.1130/G36996.1.

Chen, L., Song, X., Gerya, T.V., Xu, T., and Chen, Y., 2019, Crustal melting beneath orogenic plateaus: Insights from 3-D thermo-mechanical modeling: Tectonophysics, v. 761, 15 p., https://doi.org/10.1016/j.tecto.2019.03.014.

Colgan, J.P., and Henry, C.D., 2009, Rapid middle Miocene collapse of the Mesozoic orogenic plateau in north-central Nevada: International Geology Review, v. 51, no. 9–11, p. 920–961, https://doi.org/10.1080/00206810903056731.

Coney, P.J., and Harms, T.A., 1984, Cordilleran metamorphic core complexes: Cenozoic extensional relics of Mesozoic compression: Geology, v. 12, p. 550–554, https://doi.org/10.1130/0091-7613(1984)12<550:CMCCCE>2.0.CO;2.

Conrad, C.P., 2000, Convective instability of thickening mantle lithosphere: Geophysical Journal International, v. 143, no. 1, p 52–70, https://doi.org/10.1046/j.1365-246x.2000.00214.x.

Conrad, C.P., and Molnar, P., 1999, Convective instability of a boundary layer with temperature- and strain-rate-dependent viscosity in terms of 'available buoyancy': Geophysical Journal International, v. 139, no. 1, p. 51–68, https://doi.org/10.1046/j.1365-246X.1999.00896.x.

Cooper, F.J., Platt, J.P., Anczkiewicz, R., and Whitehouse, M.J., 2010, Footwall dip of a core complex detachment fault: Thermobarometric constraints from the northern Snake Range (Basin and Range, USA): Journal of Metamorphic Geology, v. 28, no. 9, p. 997–1020, https://doi.org/10.1111/j.1525-1314.2010.00907.x.

Cooper, F.J., Hodges, K.V., and Adams, A., 2013, Metamorphic constraints on the character and displacement of the south Tibetan fault system, central Bhutanese Himalaya: Lithosphere, v. 5, no. 1, p. 67–81, https://doi.org/10.1130/L221.1.

Crafford, A.E.J., 2007, Geologic Map of Nevada: U.S. Geological Survey Data Series, v. 249, 1 CD-ROM, 46 p.

Dahlen, F.A., 1990, Critical taper model of fold-and-thrust belts and accretionary wedges: Annual Review of Earth and Planetary Sciences, v. 18, p. 55–99, https://doi.org/10.1146/annurev.ea.18.050190.000415.

DeCelles, P.G., 2004, Late Jurassic to Eocene evolution of the Cordilleran thrust belt and foreland basin system, western U.S.A.: American Journal of Science, v. 304, no. 2, p. 105–168, https://doi.org/10.2475/ajs.304.2.105.

DeCelles, P.G., and Coogan, J.C., 2006, Regional structure and kinematic history of the Sevier fold-and-thrust belt, central Utah: Geological Society of America Bulletin, v. 118, no. 7–8, p. 841–864, https://doi.org/10.1130/B25759.1.

Dickinson, W.R., 2002, The Basin and Range Province as a composite extensional domain: International Geology Review, v. 44, no. 1, 38 p., https://doi.org/10.2747/0020-6814.44.1.1.

Dickinson, W.R., 2004, Evolution of the North American Cordillera: Annual Review of Earth and Planetary Sciences, v. 32, p. 13–45, https://doi.org/10.1146/annurev.earth.32.101802.120257.

Dickinson, W.R., 2006, Geotectonic evolution of the Great Basin: Geosphere, v. 2, no. 7, p. 353–368, https://doi.org/10.1130/GES00054.1.

Dickinson, W.R., and Snyder, W.S., 1978, Plate tectonics of the Laramide orogeny, *in* Matthews, V., III, ed., Laramide Folding Associated with Basement Block Faulting in the Western United States: Geological Society of America Memoir 151, p. 355–366, https://doi.org/10.1130/MEM151-p355.

Di Fiori, R.V., Long, S.P., Fetrow, A.C., Snell, K.E., Bonde, J.W., and Vervoort, J., 2020, Synoncontractional deposition of the cretaceous Newark canyon formation, diamond mountains, Nevada: Implications for strain partitioning within the U.S. Cordillera: Geosphere, v. 16, no. 2, p. 546–566, https://doi.org/10.1130/GES02168.1.

Douglass, W.B., Jr., 1960, Geology of the southern Butte Mountains, White Pine County, Nevada, *in* Boettcher, J.W., and Sloan, W.W., Jr., eds., Guidebook to the Geology of East-Central Nevada: Salt Lake City, Utah, Intermountain Association of Petroleum Geologists, 11th Annual Field Conference, p. 181–185.

Ducea, M.N., 2011, Fingerprinting orogenic delamination: Geology, v. 39, no. 2, p. 191–192, https://doi.org/10.1130/focus022011.1.

Ducea, M.N., Seclaman, A.C., Murray, K.E., Jianu, D., and Schoenbohm, L.M., 2013, Mantle-drip magmatism beneath the Altiplano-Puna plateau, central Andes: Geology, v. 41, no. 8, p. 915–918, https://doi.org/10.1130/G34509.1.

England, P., and Houseman, G., 1989, Extension during continental convergence, with application to the Tibetan Plateau: Journal of Geophysical Research. Solid Earth, v. 94, no. B12, p. 17,561–17,579, https://doi.org/10.1029/JB094iB12p17561.

England, P.C., and Thompson, A.B., 1984, Pressure-temperature-time paths of regional metamorphism I. Heat transfer during the evolution of regions of thickened continental crust: Journal of Petrology, v. 25, no. 4, p. 894–928, https://doi.org/10.1093/petrology/25.4.894.

Epstein, A.G., Epstein, J.B., and Harris, L.D., 1977, Conodont color alteration: An index to organic metamorphism: U.S. Geological Survey Professional Paper 995, 27 p. https://doi.org/10.3133/pp995.

Fritz, W.H., 1968, Geologic Map and Sections of the Southern Cherry Creek and Northern Egan Ranges, White Pine County, Nevada: Nevada Bureau of Mines and Geology Map 35, scale 1:62,500, 1 plate.

Fryxell, J.E., 1988, Geologic map and description of stratigraphy and structure of the west-central Grant Range, Nye County, Nevada: Geological Society of America Map Chart Series, MCH064, 16 p., 2 sheets, scale 1:24,000.

Gans, P.B., 1982, Mid-Tertiary magmatism and extensional faulting in the Hunter district, White Pine County, Nevada [Ph.D. dissertation]: Palo Alto, California, Stanford University, 3 plates, 179 p.

Gans, P.B., 1987, An open-system, two-layer crustal stretching model for the Eastern Great Basin: Tectonics, v. 6, no. 1, p. 1–12, https://doi.org/10.1029/TC006i001p00001.

Gans, P.B., and Miller, E.L., 1983, Style of mid-Tertiary extension in east-central Nevada, *in* Gurgel, K.D., ed., Geologic Excursions in the Overthrust Belt and Metamorphic Core Complexes of the Intermountain Region: Utah Geological and Mineral Survey Special Studies, v. 59, p. 107–160.

Gans, P.B., Miller, E.L., McCarthy, J., and Ouldcott, M.L., 1985, Tertiary extensional faulting and evolving ductile-brittle transition zones in the northern Snake Range and vicinity: New insights from seismic data: Geology, v. 13, no. 3, p. 189–193, https://doi.org/10.1130/0091-7613(1985)13<189:TEFAED>2.0.CO;2.

Gans, P.B., Seedorff, E., Fahey, P.L., Hasler, R.W., Maher, D.J., Jeanne, R.A., and Shaver, S.A., 2001, Rapid Eocene extension in the Robinson district, White Pine County, Nevada: Constraints from $^{40}Ar/^{39}Ar$ dating: Geology, v. 29, no. 6, p. 475–478, https://doi.org/10.1130/0091-7613(2001)029<0475:REEITR>2.0.CO;2.

Gerya, T., 2015, Tectonic overpressure and underpressure in lithospheric tectonics and metamorphism, in Deviations from Lithostatic Pressure during Metamorphism: Fact or Fiction?: Journal of Metamorphic Geology, Special Issue, v. 33, no. 8, p. 785–800, https://doi.org/10.1111/jmg.12144.

Giallorenzo, M.A., Wells, M.L., Yonkee, W.A., Stockli, D.F., and Wernicke, B.P., 2018, Timing of exhumation, Wheeler Pass thrust sheet, southern Nevada and California: Late Jurassic to middle Cretaceous evolution of the southern Sevier fold-and-thrust belt: Geological Society of America Bulletin, v. 130, no. 3-4, p. 558–579, https://doi.org/10.1130/B31777.1.

Gilbert, H., 2012, Crustal structure and signatures of recent tectonism as influenced by ancient terranes in the western United States: Geosphere, v. 8, no. 1, p. 141–157 https://doi.org/10.1130/GES00720.1.

Golding, M.L., and McMillan, R., 2020, The impacts of diagenesis on the geochemical characteristics and Color Alteration Index of conodonts: Palaeobiodiversity and Palaeoenvironments, v. 2020, p. 1–18, https://doi.org/10.1007/s12549-020-00447-y.

Gottlieb, E.S., 2017, Geologic Insights from Zircon Inheritance [Ph.D. dissertation]: Palo Alto, California, Stanford University, 354 p.

Greene, D.C., 2014, The confusion range, west-central Utah: Fold-thrust deformation and a western Utah thrust belt in the Sevier hinterland: Geosphere, v. 10, no. 1, p. 148–169, https://doi.org/10.1130/GES00972.1.

Hallett, B.W., and Spear, F.S., 2014, The P-T history of anatectic pelites of the Northern East Humboldt Range, Nevada: Evidence for tectonic loading, decompression, and anatexis: Journal of Petrology, v. 55, no. 1, p. 3–36, https://doi.org/10.1093/petrology/egt057.

Hallett, B.W., and Spear, F.S., 2015, Versatile Monazite: Resolving Geological Records and Solving Challenges in Materials Science. Monazite, zircon, and garnet growth in migmatitic pelites as a record of metamorphism and partial melting in the East Humboldt Range, Nevada: The American Mineralogist, v. 100, p. 951–972, https://doi.org/10.2138/am-2015-4839.

Harris, A.G., Wardlaw, B.R., Rust, C.C., and Merrill, G.K., 1980, Maps for assessing thermal maturity (conodont color alteration index maps) in Ordovician through Triassic rocks in Nevada and Utah and adjacent parts of Idaho and California: U.S. Geological Survey Miscellaneous Investigation Series I-1249, 2 sheets.

Henry, C.D., and John, D.A., 2013, Magmatism, ash-flow tuffs, and calderas of the ignimbrite flareup in the western Nevada volcanic field, Great Basin, USA: Geosphere, v. 9, no. 4, p. 951–1008, https://doi.org/10.1130/GES00867.1.

Henry, C.D., McGrew, A.J., Colgan, J.P., Snoke, A.W., and Brueseke, M.E., 2011, Timing, distribution, amount, and style of Cenozoic extension in the northern Great Basin, *in* Lee, J., and Evans, J.P., eds., Geologic Field Trips to the Basin and Range, Rocky Mountains, Snake River Plain, and Terranes of the U.S. Cordillera: Geological Society of America Field Guide 21, p. 27–66, https://doi.org/10.1130/2011.0021(02).

Henry, P., Le Pichon, X., and Goffé, B., 1997, Kinematic, thermal and petrological model of the Himalayas: Constraints related to metamorphism within the underthrust Indian crust and topographic elevation: Tectonophysics, v. 273, p. 31–56, https://doi.org/10.1016/S0040-1951(96)00287-9.

Hodges, K.V., and Walker, J.D., 1992, Extension in the Cretaceous Sevier Orogen, North American Cordillera: Geological Society of America Bulletin, v. 104, no. 5, p. 560–569, https://doi.org/10.1130/0016-7606(1992)104<0560:EITCSO>2.3.CO;2.

Hoiland, C., 2019, Extracting Tectonic Histories from Metamorphic Rocks in Mountain Belts: Insights from the Snake Range Metamorphic Core Complex, Nevada, and the Brooks Range, Alaska [Ph.D. dissertation]: Palo Alto, California, Stanford University, 388 p.

Hose, R.K., 1977, Structural Geology of The Confusion Range, West-Central Utah: U.S. Geological Survey Professional Paper 971, p. 97–131, https://doi.org/10.3133/pp971.
Hose, R.K., and Blake, M.C., 1976, Geology and mineral re-sources of White Pine County, Nevada, I: Geology: Nevada Bureau of Mines and Geology Bulletin, v. 85, 105 p.
Houseman, G.A., McKenzie, D.P., and Molnar, P., 1981, Convective instability of a thickened boundary-layer and its relevance for the thermal evolution of continental convergent belts: Journal of Geophysical Research, v. 86, p. 6115–6132, https://doi.org/10.1029/JB086iB07p06115.
Huerta, A.D., Royden, L.H., and Hodges, K.V., 1998, The thermal structure of collisional orogens as a response to accretion, erosion, and radiogenic heating: Journal of Geophysical Research. Solid Earth, v. 103, no. 7, p. 15,287–15,302, https://doi.org/10.1029/98JB00593.
Humphrey, F.L., 1960, Geologic Map of the White Pine Mining District, White Pine County, Nevada: Nevada Bureau of Mines and Geology Bulletin 57, scale 1:48,000, 1 plate, 67 p.
Humphreys, E.D., 1995, Post-Laramide removal of the Farallon slab, western United States: Geology, v.23, no. 11, p. 987–990, https://doi.org/10.1130/0091-7613(1995)023<0987:PLROTF>2.3.CO;2.
Hyndman, R.D., and Currie, C.A., 2011, Why is the North America Cordillera high? Hot backarcs, thermal isostasy, and mountain belts: Geology, v. 39, p. 783–786, https://doi.org/10.1130/G31998.1.
Johnston, S.M., 2000, Normal Faulting in the Upper Plate of a Metamorphic Core Complex, Northern Snake Range, Nevada [M.S. thesis]: Palo Alto, California, Stanford University, 60 p.
Kay, R.W., and Kay, S.M., 1991, Creation and destruction of lower continental crust: Geologische Rundschau, v. 80, no. 2, p. 259–278, https://doi.org/10.1007/BF01829365.
Kay, R.W., and Kay, S.M., 1993, Delamination and delamination magmatism: Tectonophysics, v. 219, p. 177–189, https://doi.org/10.1016/0040-1951(93)90295-U.
Kohn, M.J., 2014, Himalayan metamorphism and its tectonic implications: Annual Review of Earth and Planetary Sciences, v. 42, p. 381–419, https://doi.org/10.1146/annurev-earth-060313-055005.
Kohn, M.J., 2016, Metamorphic chronology - A tool for all ages: Past achievements and future prospects: The American Mineralogist, v. 101, p. 25–42, https://doi.org/10.2138/am-2016-5146.
Königshof, P., 2003, Conodont deformation patterns and textural alteration in Paleozoic conodonts: Examples from Germany and France: Senckenbergiana Lethaea, v. 83, no. 1, p. 149–156, https://doi.org/10.1007/BF03043310.
Kouketsu, Y., Mizukami, T., Mori, H., Endo, S., Aoya, M., Hara, H., and Wallis, S., 2014, A new approach to develop the Raman carbonaceous material geothermometer for low-grade metamorphism using peak width: The Island Arc, v. 23, p. 33–50, https://doi.org/10.1111/iar.12057.
Lahfid, A., Beyssac, O., Deville, E., Negro, F., Chopin, C., and Goffé, B., 2010, Evolution of the Raman spectrum of carbonaceous material in low-grade metasediments of the Glarus Alps (Switzerland): Terra Nova, v. 22, no. 5, p. 354–360, https://doi.org/10.1111/j.1365-3121.2010.00956.x.
Lee, D.E., and Fischer, L.B., 1985, Cretaceous metamorphism in the northern Snake Range, Nevada, a metamorphic core complex: Isochron-West, v. 42, p. 3–7.
Lee, D.E., Marvin, R.F., Stern, T.W., and Peterman, Z.E., 1970, Modification of potassium-argon ages by Tertiary thrusting in the Snake Range, White Pine County, Nevada: U.S. Geological Survey Professional Paper 700-D, p. D92–D102.
Lee, D.E., Marvin, R.F., and Mehnert, H.H., 1980, A radiometric age study of the Mesozoic-Cenozoic metamorphism in eastern White Pine County, Nevada, and nearby Utah: U.S. Geological Survey Professional Paper 1158-C, p. 17–28.
Lee, D.E., Stern, T.W., and Marvin, R.F., 1981, Uranium-lead-thorium isotopic ages of metamorphic monazite from the northern Snake Range, Nevada: Isochron/West, no. 31, p. 23.
Lee, D.E., Stacey, J.S.D., and Fisher, L., 1986, Muscovite-phenocrystic two-mica granites of NE Nevada are Late Cretaceous in age, *in* Shorter Contributions to Isotope Research: U.S. Geological Survey Bulletin 1622, p. 31–39.
Lee, J., Miller, E.L., and Sutter, J.F., 1987, Ductile strain and metamorphism in an extensional tectonic setting: A case study from the northern Snake Range, Nevada, USA, *in* Coward, M.P., and Dewey, J.F., Hancock, P.L., eds., Continental Extensional Tectonics: Geological Society of London, Special Publication 28, no. 1, p. 267, https://doi.org/10.1144/GSL.SP.1987.028.01.18.
Lee, J., Blackburn, T., and Johnston, S., 2017, Timing of mid-crustal ductile extension in the northern snake range metamorphic core complex, Nevada: Evidence from U/Pb zircon ages: Geosphere, v. 13, no. 2, p. 439–459, https://doi.org/10.1130/GES01429.1.
Lewis, C.J., Wernicke, B.P., Selverstone, J., and Bartley, J.M., 1999, Deep burial of the footwall of the northern Snake Range décollement, Nevada: Geological Society of America Bulletin, v. 111, no. 1, p. 39–51, https://doi.org/10.1130/0016-7606(1999)111<0039:DBOTFO>2.3.CO;2.
Long, S.P., 2012, Magnitudes and spatial patterns of erosional exhumation in the Sevier hinterland, eastern Nevada and western Utah, USA: Insights from a Paleogene paleogeologic map: Geosphere, v. 8, p. 881–901, https://doi.org/10.1130/GES00783.1.
Long, S.P., 2015, An upper-crustal fold province in the hinterland of the Sevier orogenic belt, eastern Nevada, U.S.A.: A Cordilleran Valley and Ridge in the Basin and Range: Geosphere, v. 11, p. 404–424, https://doi.org/10.1130/GES01102.1.
Long, S.P., 2019, Geometry and magnitude of extension in the Basin and Range Province (39°N), Utah, Nevada, and California, USA: Constraints from a province-scale cross section: Geological Society of America Bulletin, v. 131, p. 99–119, https://doi.org/10.1130/B31974.1.
Long, S.P., and Soignard, E., 2016, Shallow-crustal metamorphism during Late Cretaceous anatexis in the Sevier hinterland plateau: Peak temperature conditions from the Grant Range, eastern Nevada, U.S.A: Lithosphere, v. 8, p. 150–164, https://doi.org/10.1130/L501.1.
Long, S.P., and Walker, J.P., 2015, Geometry and kinematics of the Grant Range brittle detachment system, eastern Nevada, USA: An end-member style of upper crustal extension: Tectonics, v. 34, no. 9, p. 1837–1862, https://doi.org/10.1002/2015TC003918.
Long, S.P., Henry, C.D., Muntean, J.L., Edmondo, G.P., and Cassel, E.J., 2014a, Early Cretaceous construction of a structural culmination, Eureka, Nevada, U.S.A.: Implications for out-of-sequence deformation in the Sevier hinterland: Geosphere, v. 10, no. 3, p. 564–584, https://doi.org/10.1130/GES00997.1.
Long, S.P., Henry, C.D., Muntean, J.L., Edmondo, G.P., and Thomas, R.D., 2014b, Geologic Map of the Southern Part of the Eureka Mining District and Surrounding Areas of the Fish Creek Range, Mountain Boy Range, and Diamond Mountains, Eureka and White Pine Counties, Nevada: Nevada Bureau of Mines and Geology Map 183, scale 1:24,000, 2 plates, 36 p.
Long, S.P., Thomson, S.N., Reiners, P.W., and Di Fiori, R.V., 2015, Synorogenic extension localized by upper-crustal thickening: An example from the Late Cretaceous Nevadaplano: Geology, v. 43, no. 4, p. 351–354, https://doi.org/10.1130/G36431.1.
Long, S.P., Heizler, M.T., Thomson, S.N., Reiners, P.W., and Fryxell, J.E., 2018, Rapid Oligocene to Early Miocene Extension Along the Grant Range Detachment System, Nevada, USA: Insights From Multipart Cooling Histories of Footwall Rocks: Tectonics, v. 37, no. 12, p. 4752–4779, https://doi.org/10.1029/2018TC005073.
Lund, K., Beard, L.S., and Perry, W.J., 1993, Relation between extensional geometry of the northern Grant Range and oil occurrences in Railroad Valley, east-central Nevada: American Association of Petroleum Geologists Bulletin, v. 77, no. 6, 962 p., https://doi.org/10.1306/bdff8da8-1718-11d7-8645000102c1865d.
Lünsdorf, N.K., and Lünsdorf, J.O., 2016, Evaluating Raman spectra of carbonaceous matter by automated, iterative curve-fitting: International Journal of Coal Geology, v. 160, p. 51–62, https://doi.org/10.1016/j.coal.2016.04.008.
Lünsdorf, N.K., Dunkl, I., Schmidt, B.C., Rantitsch, G., and von Eynatten, H., 2017, Towards a higher comparability of geothermometric data obtained by Raman spectroscopy of carbonaceous material. Part 2: A revised geothermometer: Geostandards and Geoanalytical Research, v. 41, no. 4, p. 593–612, https://doi.org/10.1111/ggr.12178.
McGrew, A.J., Peters, M.T., and Wright, J.E., 2000, Thermobarometric constraints on the tectonothermal evolution of the East Humboldt range metamorphic core complex, Nevada: Geological Society of America Bulletin, v. 112, p. 45–60, https://doi.org/10.1130/0016-7606(2000)112<45:TCOTTE>2.0.CO;2.
McMillan, R., and Golding, M., 2019, Thermal maturity of carbonaceous material in conodonts and the Color Alteration Index: Independently identifying maximum temperature with Raman spectroscopy: Palaeogeography, Palaeoclimatology, Palaeoecology, v. 534, no. 109290, https://doi.org/10.1016/j.palaeo.2019.109290.
Miller, D.M., and Hoisch, T.D., 1995, Jurassic tectonics of northeastern Nevada and northwestern Utah from the perspective of barometric studies, *in* Miller, D.M., and Busby, C., eds., Jurassic Magmatism and Tectonics of the North American Cordillera: Geological Society of America Special Paper 299, p. 267–294, https://doi.org/10.1130/SPE299-p267.
Miller, E.L., and Gans, P.B., 1989, Cretaceous crustal structure and metamorphism in the hinterland of the Sevier thrust belt, western U.S. Cordillera: Geology, v. 17, no. 1, p. 59–62, https://doi.org/10.1130/0091-7613(1989)017<0059:CCSAMI>2.3.CO;2.
Miller, E.L., Gans, P.B., and Garing, J., 1983, The Snake Range Décollement: An exhumed Mid-Tertiary ductile-brittle transition: Tectonics, v. 2, no. 3, p. 239–263, https://doi.org/10.1029/TC002i003p00239.
Miller, E.L., Gans, P.B., Wright, J.E., and Sutter, J.F., 1988, Metamorphic history of the east-central Basin and Range province: Tectonic setting and relationship to magmatism, *in* Ernst, W.G., ed., Metamorphism and Crustal Evolution, Western Conterminous United States: Englewood Cliffs, New Jersey, Prentice-Hall, p. 649–682.
Molnar, P., Houseman, G.A., and Conrad, C.P., 1998, Rayleigh-Taylor instability and convective thinning of mechanically thickened lithosphere: Effects of non-linear viscosity decreasing

exponentially with depth and of horizontal shortening of the layer: Geophysical Journal International, v. 133, no. 3, p. 568–584, https://doi.org/10.1046/j.1365-246X.1998.00510.x.
Morency, C., and Doin, M.P., 2004, Numerical simulations of the mantle lithosphere delamination: Journal of Geophysical Research, v. 109, no. B3, B03410, https://doi.org/10.1029/2003JB002414.
Nelson, R.B., 1966, Structural Development of Northernmost Snake Range, Kern Mountains, and Deep Creek Range, Nevada and Utah: American Association of Petroleum Geologists Bulletin, v. 50, no. 5, 951 p., https://doi.org/10.1306/5d25b605-16c1-11d7-8645000102c1865d.
Nolan, T.B., Merriam, C.W., and Blake, M.C., Jr., 1974, Geologic Map of the Pinto Summit Quadrangle, Eureka and White Pine Counties, Nevada: U.S. Geological Survey Miscellaneous Investigations Series Map I-793, scale 1:31,680, 2 plates, 14 p.
Oldow, J.S., Bally, A.W., Ave Lallemant, H.G., and Leeman, W.P., 1989, Phanerozoic evolution of the North American Cordillera: United States and Canada, *in* Bally, A.W., and Palmer, A.R., eds., The Geology of North America—An Overview, v. A: Boulder, Colorado, Geological Society of America, p. 139–232, https://doi.org/10.1130/DNAG-GNA-A.139.
Oldow, J.S., Bally, A.W., and Ave Lallemant, H.G., 1990, Transpression, orogenic float, and lithospheric balance: Geology, v. 18, no. 10, p. 991–994, https://doi.org/10.1130/0091-7613(1990)018<0991:TOFALB>2.3.CO;2.
Petrini, K., and Podladchikov, Y., 2000, Lithospheric pressure-depth relationship in compressive regions of thickened crust: Journal of Metamorphic Geology, v. 18, no. 1, p. 67–77, https://doi.org/10.1046/j.1525-1314.2000.00240.x.
Poole, F.G., Stewart, J.H., Palmer, A.R., Sandberg, C.A., Madrid, R.J., Ross, R.J., Jr., Hintze, L.F., Miller, M.M., and Wricke, C.T., 1992, Latest Precambrian to latest Devonian time: Development of a continental margin, *in* Burchfiel, B.C., Lipman, P.W., and Zoback, M.L., eds., The Cordilleran Orogen: Conterminous U.S.: Boulder, Colorado, Geological Society of America, The Geology of North America, v. G-3, p. 9–56, https://doi.org/10.1130/DNAG-GNA-G3.9.
Proffett, J.M., 1977, Cenozoic geology of the Yerington district, Nevada, and implications for the nature and origin of Basin and Range faulting: Bulletin of the Geological Society of America, v. 88, no. 2, p. 247–266, https://doi.org/10.1130/0016-7606(1977)88<247:CGOTYD>2.0.CO;2.
Putney, T.R., 1985, Geology, geochemistry, and alteration of the Seligman and Monte Crista stocks, White Pine Mining District, White Pine County, Nevada [M.S. thesis]: University of Reno, Nevada, 152 p.
Rahl, J.M., Anderson, K.M., Brandon, M.T., and Fassoulas, C., 2005, Raman spectroscopic carbonaceous material thermometry of low-grade metamorphic rocks: Calibration and application to tectonic exhumation in Crete, Greece: Earth and Planetary Science Letters, v. 240, no. 2, p. 339–354, https://doi.org/10.1016/j.epsl.2005.09.055.
Rodgers, D.W., 1987, Thermal and structural evolution of the southern Deep Creek Range, west central Utah and east central Nevada [Ph.D. dissertation]: Palo Alto, California, Stanford University, 5 plates, 149 p.
Rosenberg, C.L., and Handy, M.R., 2005, Experimental deformation of partially melted granite revisited: Implications for the continental crust: Journal of Metamorphic Geology, v. 23, p. 19–28, https://doi.org/10.1111/j.1525-1314.2005.00555.x.
Royden, L.H., 1993, The steady state thermal structure of eroding orogenic belts and accretionary prisms: Journal of Geophysical Research, v. 98, p. 4487–4507, https://doi.org/10.1029/92JB01954.
Saleeby, J., and Foster, Z., 2004, Topographic response to mantle lithosphere removal in the southern Sierra Nevada region, California: Geology, v. 32, no. 3, p. 245–248, https://doi.org/10.1130/G19958.1.
Schmalholz, S.M., and Podladchikov, Y.Y., 2013, Tectonic overpressure in weak crustal-scale shear zones and implications for the exhumation of high-pressure rocks: Geophysical Research Letters, v. 40, no. 10, p. 1984–1988, https://doi.org/10.1002/grl.50417.
Schott, B., and Schmeling, H., 1998, Delamination and detachment of a lithospheric root: Tectonophysics, v. 296, p. 225–247, https://doi.org/10.1016/S0040-1951(98)00154-1.
Smith, M.E., Carroll, A.R., Jicha, B.R., Cassel, E.J., and Scott, J.J., 2014, Paleogeographic record of Eocene Farallon slab rollback beneath western North America: Geology, v. 42, no. 12, p. 1039–1042, https://doi.org/10.1130/G36025.1.
Snell, K.E., Koch, P.L., Druschke, P., Foreman, B.Z., and Eiler, J.M., 2014, High elevation of the "Nevadaplano" during the Late Cretaceous: Earth and Planetary Science Letters, v. 386, p. 52–63, https://doi.org/10.1016/j.epsl.2013.10.046.
Sonnevil, R.A.,1979, Evolution of skarn at Monte Cristo, Nevada [M.S. thesis]: Palo Alto, California, Stanford University, 84 p.
Spear, F.S., Kohn, M.J., and Cheney, J.T., 1999, P-T paths from anatectic pelites: Contributions to Mineralogy and Petrology, v. 134, no. 1, p. 17–32, https://doi.org/10.1007/s004100050466.
Speed, R.C., and Sleep, N.H., 1982, Antler orogeny and foreland basin: A model (Nevada, Idaho): Geological Society of America Bulletin, v. 93, no. 9, p. 815–828, https://doi.org/10.1130/0016-7606(1982)93<815:AOAFBA>2.0.CO;2.
Stewart, J.H., 1980, Geology of Nevada: Nevada Bureau of Mines and Geology, Special Publication 4, 136 p.
Stewart, J.H., and Carlson, J.E., 1978, Generalized maps showing distribution, lithology, and age of Cenozoic igneous rocks in the Western United States, *in* Smith, R.B., and Eaton, G.P., eds., Cenozoic Tectonics and Regional Geophysics of the Western Cordillera: Geological Society of America Memoir 152, p. 263–264, https://doi.org/10.1130/MEM152-p263.
Stewart, J.H., and Poole, F.G., 1974, Lower Paleozoic and Uppermost Precambrian Cordilleran Miogeocline, Great Basin, Western United States, *in* Dickinson, W.R., Tectonics and Sedimentation: SEPM Special Publication, v. 22, https://doi.org/10.2110/pec.74.22.0028.
Stipp, M., Stünitz, H., Heilbronner, R., and Schmid, S.M., 2002, The eastern Tonale fault zone: A "natural laboratory" for crystal plastic deformation of quartz over a temperature range from 250 to 700 °C: Journal of Structural Geology, v. 24, p. 1861–1884, https://doi.org/10.1016/S0191-8141(02)00035-4.
Suppe, J., 1983, Geometry and kinematics of fault-bend folding: American Journal of Science, v. 283, no. 7, p. 684-721, https://doi.org/10.2475/ajs.283.7.684.
Suppe, J., and Medwedeff, D.A., 1990, Geometry and kinematics of fault-propagation folding: Eclogae Geologicae Helvetiae, v. 83, no. 3, p. 409–454, https://doi.org/10.5169/seals-166595.
Surpless, B.E., Stockli, D.F., Dumitru, T.A., and Miller, E.L., 2002, Two-phase westward encroachment of Basin and Range extension into the northern Sierra Nevada: Tectonics, v. 21, no. 1, p. 2-1–2-10, https://doi.org/10.1029/2000TC001257.
Taylor, W.J., Bartley, J.M., Fryxell, J.E., Schmitt, J., and Vandervoort, D.S., 1993, Mesozoic Central Nevada thrust belt, *in* Lahren, M.M., Trexler, J.H., and Spinosa, C., eds., Crustal Evolution of the Great Basin and the Sierra Nevada: Reno, Nevada, Department of Geological Sciences, Mackay School of Mines, University of Nevada, p. 57–96.
Taylor, W.J., Bartley, J.M., Martin, M.W., Geissman, J.W., Walker, J.D., Armstrong, P.A., and Fryxell, J.E., 2000, Relations between hinterland and foreland shortening: Sevier orogeny central North American Cordillera: Tectonics, v. 19, no. 6, p. 1124–1143, https://doi.org/10.1029/1999TC001141.
Thorman, C.H., Ketner, K.B., Brooks, W.E., Snee, L.W., Zimmerman, R.A., and Raines, G.L., 1991, Late Mesozoic–Cenozoic tectonics in northeastern Nevada, *in* Geology and Ore Deposits of the Great Basin: Reno, Nevada, Symposium Proceedings, Geological Society of Nevada, p. 25–45.
Wells, M.L., and Hoisch, T.D., 2008, The role of mantle delamination in widespread Late Cretaceous extension and magmatism in the Cordilleran orogen, western United States: Geological Society of America Bulletin, v. 120, no. 5–6, p. 515–530. https://doi.org/10.1130/B26006.1.
Wells, M.L., Hoisch, T.D., Cruz-Uribe, A.M., and Vervoort, J.D., 2012, Geodynamics of synconvergent extension and tectonic mode switching: Constraints from the Sevier-Laramide orogen: Tectonics, v. 31, p. 1–20, https://doi.org/10.1029/2011TC002913.
West, J.D., Fouch, M.J., Roth, J.B., and Elkins-Tanton, L.T., 2009, Vertical mantle flow associated with a lithospheric drip beneath the Great Basin: Nature Geoscience, v. 2, p. 439–444, https://doi.org/10.1038/ngeo526.
Yao, W.H., Li, Z.X., Li, W.X., Wang, X.C., Li, X.H., and Yang, J.H., 2012, Post-kinematic lithospheric delamination of the Wuyi-Yunkai orogen in South China: Evidence from ca. 435 Ma high-Mg basalts: Lithos, v. 154, p. 115–129, https://doi.org/10.1016/j.lithos.2012.06.033.
Yonkee, W.A., and Weil, A.B., 2015, Tectonic evolution of the Sevier and Laramide belts within the North American Cordillera orogenic system: Earth-Science Reviews, v. 150, p. 531–593, https://doi.org/10.1016/j.earscirev.2015.08.001.
Young, J.C., 1960, Structure and Stratigraphy in the North-Central Schell Creek Range, Eastern Nevada [Ph.D. dissertation]: Princeton, New Jersey, Princeton University, 207 p., 3 plates.
Zuza, A.V., Thorman, C., Henry, C., Levy, D., Dee, S., Long, S., Sandberg, C., and Soignard, E., 2020a, Pulsed Mesozoic Deformation in the Cordilleran Hinterland and Evolution of the Nevadaplano: Insights from the Pequop Mountains, NE Nevada: Lithosphere, v. 2020, p. 1–24, https://doi.org/10.2113/2020/8850336.
Zuza, A.V., Levy, D.A, and Mulligan, S., 2020b, Geologic field evidence for non-lithostatic overpressure recorded in the North American Cordillera hinterland, northeast Nevada: Geoscience Frontiers, 101099, https://doi.org/10.1016/j.gsf.2020.10.006.